Solid State Nuclear Magnetic Resonance 140 (2025) 102034

Contents lists available at ScienceDirect

Solid State Nuclear Magnetic Resonance

journal homepage: www.elsevier.com/locate/ssnmr

# *De novo* crystal structure determination of *L*-alaninamide HCl by quadrupolar NMR crystallography guided crystal structure prediction (QNMRX-CSP)

Carl H. Fleischer III [a,b], Sean T. Holmes [a,b], Xinsong Lin [a], Robert W. Schurko [a,b,*]

[a] Department of Chemistry & Biochemistry, Florida State University, Tallahassee, FL, 32306, USA
[b] National High Magnetic Field Laboratory, Tallahassee, FL, 32310, USA

ARTICLE INFO

Handling Editor: Prof D Bryce

ABSTRACT

Quadrupolar NMR crystallography guided crystal structure prediction (QNMRX-CSP) is a method for determining the crystal structures of organic solids. To date, our two previous QNMRX-CSP studies have relied upon on $^{35}$Cl solid-state NMR (SSNMR) spectroscopy, powder X-ray diffraction (PXRD), Monte-Carlo simulated annealing (MC-SA), and dispersion-corrected density functional theory (DFT-D2*) calculations for the determination of crystal structures for organic HCl salts with known crystal structures, in order to benchmark the method and subject it to blind tests. Herein, we apply QNMRX-CSP for the *de novo* crystal structure determination of *L*-alaninamide HCl (*L*-Ala-$NH_2$), for which no crystal structure has been reported, using $^{35}$Cl SSNMR and PXRD data for structural prediction and refinement, along with $^{13}$C and $^{14}$N SSNMR data for subsequent structural validation. To further validate our structural models, we determined the crystal structure of *L*-Ala-$NH_2$ using single-crystal X-ray diffraction (SCXRD); however, this structure was not obtained until the completion of the QNMRX-CSP analysis and validation. This study highlights the current capabilities of QNMRX-CSP and underscores the benefits of incorporating multinuclear SSNMR data to enhance *de novo* crystal structure determination across a wide range of organic solids.

## 1. Introduction

There is widespread interest in the structural characterization of organic solids, as evidenced by the over 1.3 million crystal structures deposited in the Cambridge Structural Database (CSD) [1,2]. Most of these structures were determined using single crystal X-ray diffraction (SCXRD); however, not all materials are amenable to investigation by this method. For instance, organic solids produced by mechanochemistry often yield micro- or nanocrystalline powders from which crystals suitable for SCXRD cannot be obtained [3]. In such instances, Rietveld refinement of powder X-ray diffraction (PXRD) data can be used for structural determination; however, this is challenging, especially in the absence of key chemical and crystallographic information. Furthermore, several factors preceding Rietveld refinements, including determination of the space group and unit cell parameters, as well as the selection of a reasonable initial structural model, are fraught with difficulties; notably, poor quality PXRD patterns and the presence of mixed and/or impurity phases that cause peak overlap are common obstacles [4,5].

Crystal structure prediction (CSP) methods have revolutionized the ability to determine crystal structures without relying solely on experimental data [6–12], and are eminently suited for integration with Riet-veld refinements, both for generating initial structural models and identifying the most probable candidate structures [13–18]. CSP methods offer a variety of strategies for generating high-quality structural models [19–25]; however, most approaches follow a common workflow that first generates a pool of structural candidates, followed by their ranking using key metrics such as calculated static lattice energies [26–29]. However, differences in static lattice energies between solid forms often fall within the anticipated error margins of quantum chemical computations, making it challenging to distinguish among structures based solely on these energies [30,31]. Therefore, it is useful to incorporate experimental data that capture molecular, electronic, and crystal structural features in the solid state. Solid-state NMR (SSNMR) spectroscopy can provide such insights, playing a pivotal role in

This article is part of a special issue entitled: Advancements in SSNMR published in Solid State Nuclear Magnetic Resonance.

* Corresponding author. Department of Chemistry & Biochemistry, Florida State University, Tallahassee, FL 32306, USA.
*E-mail address:* rschurko@fsu.edu (R.W. Schurko).

https://doi.org/10.1016/j.ssnmr.2025.102034
Received 29 May 2025; Received in revised form 21 July 2025; Accepted 21 August 2025
Available online 22 August 2025

determining crystal structures.

NMR crystallography (NMRX) is an integrated approach combining SSNMR, diffraction methods, and quantum chemical computations to determine structures of crystalline materials [32–39]. Unlike conventional crystallographic approaches based on XRD or neutron diffraction data, NMRX can leverage data from a broader range of sample types, such as microcrystalline powders and amorphous solids.

The majority of NMRX studies exploit chemical shifts as their primary metric, owing to their sensitivity to local structural environments, ease of accurate measurement, and reliability of predictions using quantum chemical computations [33,34,37,40]. Because chemical shifts reflect subtle variations in bonding, conformation, and intermolecular interactions, they are well-suited for ranking candidate structural models generated by CSP methods [41–44]. In particular, plane-wave density functional theory (DFT) methods have enabled quantitative comparison between experimental and calculated chemical shifts [36, 38,39,45]. Unfortunately, DFT calculations of chemical shifts can be computationally expensive, and therefore, should be limited to only the best structural models, including those obtained from CSP methods and even Rietveld refinements. To overcome these limitations, Emsley and co-workers have introduced ShiftML2 [46,47], a machine learning model capable of predicting chemical shifts for crystalline materials [48–50] and amorphous solids [51,52] with speeds several orders of magnitude faster than DFT methods.

Quadrupolar interaction parameters, which manifest in the SSNMR powder patterns of quadrupolar nuclides (*i.e.*, nuclear spins $I > ½$), are of great utility in NMRX. Quadrupolar nuclei comprise *ca.* 73 % of stable NMR-active isotopes, affording myriad opportunities for the study of a wide range of materials [53]. The quadrupolar interaction originates from the coupling between the nuclear quadrupole moment and the electric field gradients (EFG) at the nucleus. EFGs are described by a traceless, second-rank tensor, which in its own principal axis system is defined by three principal components along the diagonal, ranked such that $|V_{33}| \geq |V_{22}| \geq |V_{11}|$. The relative values of these components are expressed using the quadrupolar coupling constant, $C_Q = eQV_{33}/h$, and the quadrupolar asymmetry parameter, $\eta_Q = (V_{11} - V_{22})/V_{33}$, where $e$ is the elementary charge, $h$ is Planck's constant, $Q$ is the nuclear quadrupole moment, and $0 \leq \eta_Q \leq 1$. Since the EFGs depend solely on the ground state electronic density, they can be calculated rapidly compared to chemical shifts using DFT methods [54,55].

There have been relatively few NMRX studies utilizing EFG tensors [56–64] in comparison to those employing chemical shifts. In part, this can be attributed to the difficulties in accurately calculating EFG tensors due to their long-range dependence on ground-state electron density. In particular, the positioning of hydrogen atoms and validity of their associated bonding descriptions represent major issues for calculations of EFG tensors for organic [65,66], biological [67], inorganic [68], and hybrid compounds and materials [69], especially when hydrogen bonding or other weak van der Waals interactions influence the EFG tensor parameters and orientations [54,55,66,70,71].

Our group has introduced a dispersion-corrected DFT method, DFT-D2*, for the geometry optimization of structures of solid organic compounds [65,66]. DFT-D2* calculations provide accurate atomic positions for both heavy and light atoms, which in turn, facilitates accurate calculations of EFG and magnetic shielding tensors. This greatly assisted in the development of quadrupolar NMR crystallography guided crystal structure prediction (QNMRX-CSP) [63,64], which to date has relied upon accurate measurements and calculations of $^{35}$Cl EFG tensors for determining the crystal structures of organic HCl salts.

QNMRX-CSP has been used to determine the most probable structural candidates of nine organic HCl salts featuring relatively small, rigid, organic components [63,64]. This early work involved benchmarking key metrics that are used to rank candidate structures [63], blind structural prediction tests on several systems, and exploring options for structural determination in cases where unit cell parameters and space groups are unavailable [64]. These studies have been limited to organic HCl salts with known crystal structures and used $^{35}$Cl EFG tensors as the sole NMR-based metric for structural determination. Our ongoing work endeavors to explore organic HCl salts for which crystal structures are unknown, including those with more complex organic components. These efforts can be aided by multinuclear SSNMR data from other nuclides that are generally found in organic HCl salts (*i.e.*, $^{13}$C, $^{14}$N, and $^{17}$O, etc.) [42,72–76], since such data shows promise for ranking structural candidates [77,78].

Herein, we apply QNMRX-CSP for the *de novo* determination of the structure of *L*-alaninamide HCl (*L*-Ala-$NH_2$). Key experimental data include the $^{35}$Cl EFG tensors derived from $^{35}$Cl SSNMR spectra, as well as the space group, unit cell parameters, and $Z'$ determined from PXRD data. The structural models of *L*-Ala-$NH_2$ were validated using multinuclear SSNMR data ($^{13}$C and $^{14}$N) and determined independently by SCXRD analysis – the latter of which was not revealed until after we were satisfied that a valid structural candidate had emerged from QNMRX-CSP. Finally, we posit future possibilities for QNMRX-CSP studies that incorporate data from multiple spin-1/2 and quadrupolar nuclides, including the combined use of chemical shifts and EFG tensors.

## 2. Methods

### 2.1. Materials

*L*-Ala-$NH_2$ was purchased from Sigma Aldrich and recrystallized from aqueous solution to obtain crystals suitable for analysis by SCXRD. Prior to analysis by PXRD and SSNMR, crystals were ball-milled in 10 mL stainless steel jars using one 7 mm stainless steel ball bearing at a milling frequency of 30 Hz for 10 min.

### 2.2. Single-crystal X-ray diffraction

A clear crystal of *L*-Ala-$NH_2$ was mounted on a nylon loop with perfluoroether oil. Data was collected from this single crystal at 295(3) K on an XtaLAB Synergy, Dualflex, HyPix four-circle diffractometer with a micro-focus sealed X-ray tube using a mirror as monochromator and a HyPix detector. The diffractometer is equipped with an Oxford Cryostream 800 low-temperature device and uses Cu *K*α radiation. The structure was solved by dual methods using SHELXT and refined by full-matrix least-squares methods against $F^2$ by SHELXL (Table S1) [79,80]. All non-hydrogen atoms were refined with anisotropic displacement parameters. All carbon-bound hydrogen atoms were refined isotropically on calculated positions using a riding model, with their $U_{iso}$ values constrained to 1.5 times the $U_{eq}$ of their pivot atoms for terminal $sp^3$ carbon atoms and 1.2 times for all other carbon atoms.

### 2.3. Powder X-ray diffraction

A PXRD pattern of *L*-Ala-$NH_2$ (Fig. 1A) was acquired using a Rigaku SmartLab X-ray diffractometer operating with Bragg-Brentano geometry and featuring a Cu *K*α radiation source and a D/tex Ultra 250 1D silicon strip detector. The X-ray tube voltage and amperage were 40 kV and 15 mA, respectively. Diffraction patterns were acquired with a detector scanning 2θ from 5° to 50° with a step size of 0.01° and at a rate of 0.5° $min^{-1}$. The PXRD pattern was background-corrected and smoothed using a width of 0.01 and was indexed (Table 1) in the Reflex Powder Index in BIOVIA Materials Studio 2020 R3 employing the X-Cell scheme [81]. Indexing used the Simple detection method starting from 5° with the maximum number of peaks set to 50 and a low amplitude cutoff of 2.0 %.

### 2.4. Solid-state NMR

SSNMR spectra were acquired at 14.1 T and 18.8 T at the National High Magnetic Field Laboratory (NHMFL) in Tallahassee, FL using Bruker Avance NEO spectrometers and Oxford standard or wide bore

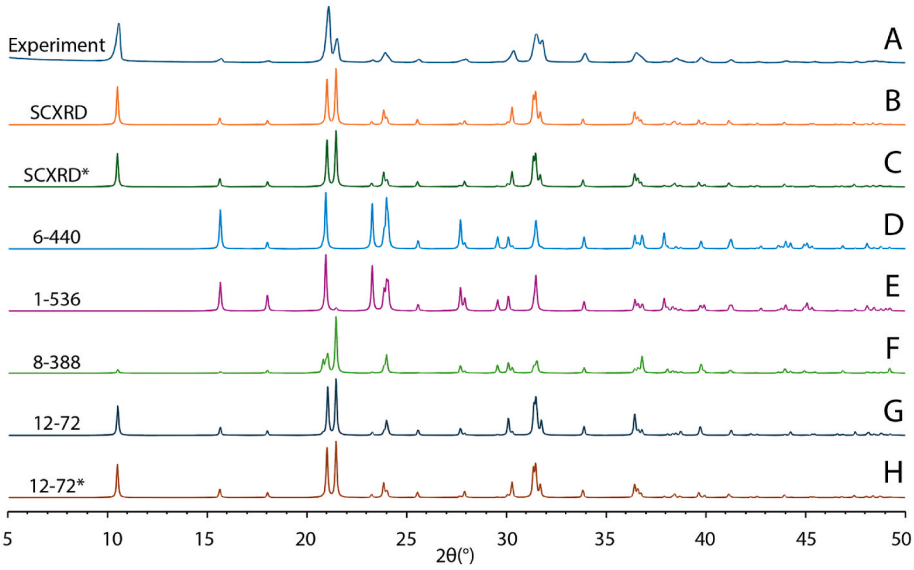


**Fig. 1.** (A) Experimental PXRD pattern of *L*-Ala-$NH_2$ (Experiment); (B) simulated PXRD patterns of the SCXRD structure (SCXRD); (C) DFT-D2* geometry-optimized SCXRD structure (SCXRD*); QNMRX-CSP structural models for (D) 6–440, (E) 1–536, (F) 8–388, and (G) 12–72; and (H) structural model 12–72 with unit cell parameters matching those obtained from SCXRD and DFT-D2* geometry optimization (12–72*).

**Table 1**
Crystallographic information for *L*-Ala-$NH_2$.[a]

| | Space Group | *a* (Å) | *b* (Å) | *c* (Å) | α (°) | β (°) | γ (°) |
|---|---|---|---|---|---|---|---|
| PXRD (Indexed) | $P2_1$ | 4.9327(234) | 7.6518(150) | 8.4543(239) | 90 | 90.441(239) | 90 |
| SCXRD | $P2_1$ | 4.9305(3) | 7.6612(5) | 8.4690(5) | 90 | 90.491(6) | 90 |

[a] The experimental uncertainties in the last digits for each value are indicated in parentheses.

magnets, where the relevant Larmor frequencies at 14.1 T are $\nu_0(^1H)$ = 600.07 MHz, $\nu_0(^{13}C)$ = 150.87 MHz, and $\nu_0(^{35}Cl)$ = 58.795 MHz, and at 18.8 T are $\nu_0(^1H)$ = 800.13 MHz, $\nu_0(^{14}N)$ = 57.799 MHz, and $\nu_0(^{35}Cl)$ = 78.396 MHz. All experiments used NHMFL-built 3.2 mm HXY MAS probes with samples packed into 3.2 mm o.d. zirconia rotors. Spectra were processed and fit using the ssNake v1.3 software package [82]. Relevant acquisition parameters are provided in Table S2–S4.

**$^{35}$Cl{$^1$H} Experiments**. $^{35}$Cl{$^1$H} spectra were acquired under static conditions at 14.1 T and both static and MAS conditions at 18.8 T using the Hahn-echo pulse sequence [83,84] with 2.5 μs CT-selective π/2 pulses and a $^1$H decoupling field of 50 kHz. MAS spectra were acquired using a MAS rate of $\nu_{rot}$ = 10 kHz. $^{35}$Cl chemical shifts were referenced to 0.1 M NaCl (aq) at $\delta_{iso}(^{35}Cl)$ = 0.0 ppm using the chemical shift of NaCl (s) at $\delta_{iso}(^{35}Cl)$ = −41.11 ppm as a secondary reference. [85].

**$^{14}$N{$^1$H} Experiments**. $^{14}$N{$^1$H} spectra were acquired under static conditions at 18.8 T using the WURST-CPMG pulse sequence [86–89]. 50 μs WURST-80 pulses with a maximum amplitude of $\nu_1(^{14}N)$ = 50 kHz were swept from low to high frequency with a sweep width of 1.0 MHz. A $^1$H decoupling field of 50 kHz was applied. Due to the large pattern breadth, the spectrum was acquired by stepping the transmitter in 100 kHz increments up to a transmitter offset of 500 kHz (*i.e.*, five sub-spectra, following the variable-offset cumulative spectra (VOCS) method) [90]. Sub-spectra were collected only on the high-frequency side of the pattern, since it is symmetric about 0 kHz due to the dominance of the first-order quadrupolar interaction and minimal effects of nitrogen chemical shift anisotropy [91]. The low-frequency side of the spectra is obtained by "reflecting" the spectra obtained on the high-frequency side through the position of the transmitter frequency. $^{14}$N chemical shifts were referenced relative to $NH_4Cl$ at $\delta_{iso}(^{14}N)$ = 0.0 ppm, although the $\delta_{iso}$ values are not reported due to their inherently high uncertainties.

**$^1$H→$^{13}$C{$^1$H} Experiments**. The $^1$H→$^{13}$C{$^1$H} variable-amplitude CP/MAS pulse sequence [92–96] was used to obtain the $^{13}$C SSNMR spectra at 14.1 T. Spectra were acquired using $^1$H π/2 pulses of 2.5 μs, a contact time of 1 ms, a 50 kHz $^1$H and 42 kHz $^{13}$C Hartmann-Hahn match, SPINAL-64 $^1$H decoupling ($\nu_2$ = 100 kHz), and a spinning rate of 10 kHz. $^{13}$C chemical shifts were referenced to TMS at $\delta_{iso}(^{13}C)$ = 0.0 ppm using the high frequency peak of α-glycine at $\delta_{iso}(^{13}C)$ = 176.5 ppm as a secondary reference. [97].

### 2.5. QNMRX-CSP

QNMRX-CSP (Scheme S1) consists of three modules for the structural determination of *L*-Ala-$NH_2$: (i) Module 1 (M1) develops a "chemically sensible" *L*-Ala-$NH_2$ molecular fragment; (ii) Module 2 (M2) employs Polymorph to produce the initial candidate structures; and (iii) Module 3 (M3) uses QNMRX to refine and validate the candidate structures. Calculations performed in the three modules are detailed below. In M2 and M3, candidate structures are retained using metric sets, which are detailed in **§2.6** and Table 2. Candidate structures are validated using the parameters detailed in **§2.7**.

QNMRX-CSP [63,64] was designed and benchmarked for the crystal structure determination of small organic HCl salts using a combination of (i) PXRD (**§2.3**), (ii) $^{35}$Cl SSNMR (**§2.4**), and (iii) quantum chemical computations. For the latter, two graphical user interfaces are used: (i) BIOVIA Materials Studio 2020 R3 interacts with Polymorph [98] and CASTEP [99]; and (ii) CASTEP Data Manager interacts with the standalone academic version of CASTEP 2020 to automate calculations and data analysis. In addition to QNMRX-CSP, NMR parameters ($^{13}$C chemical shifts and $^{14}$N EFG tensors) are calculated for the candidate structures using CASTEP [99] and ShiftML2 [47] for structural validation (**§2.7**).

**Table 2**
QNMRX-CSP Metric Sets and the benchmarked metric thresholds.

| Metric Set | Unit cell parameters[a] | $E_{lat}$[b] | $\Gamma_{EFG}$ (MHz)[c] | $E_{thresh}$ (kJ mol$^{-1}$)[d] |
|---|---|---|---|---|
| 1 | ±20 % | 13.5 % | – | – |
| 2 | – | – | 0.70 | 135 |
| 3 | – | – | 0.49 | 50/60.52[e] |
| 4 | – | – | 0.49 | 1 |

[a] Candidate structures are retained if their unit cell parameters are within ±20 % of the indexed unit cell parameters.
[b] Candidate structures in the bottom 13.5 % of $E_{lat}$ values are retained, *i.e.*, those in the regime $E_{low} \leq E_{lat} \leq 0.865 \cdot E_{low}$.
[c] Candidate structures are retained if their $\Gamma_{EFG}$ is equal to or below the benchmarked threshold.
[d] Candidate structures are retained if their $E_{lat}$ is equal to or below the energy threshold, such that $E_{lat} - E_{low} \leq E_{thresh}$.
[e] In Metric Set 3, $E_{thresh}$ was initially set to equal 50 kJ mol$^{-1}$ and was later reevaluated to 60.52 kJ mol$^{-1}$. For further discussion see **§3.2**.

#### 2.5.1. Polymorph

Polymorph generates the candidate structures of *L*-Ala-$NH_2$ and requires three inputs, including the (i) space group, (ii) motion groups, and (iii) atomic Hirshfeld charges (see **§2.5.2**). The motion groups are assigned as a $Cl^-$ ion and an organic cation, the latter of which has been geometry-optimized using DFT-D2* (**§2.5.2**). Polymorph employs a four-step routine to generate a maximum of 10,000 candidate structures per trial. A trial consists of one complete iteration of (i) packing, (ii) clustering, (iii) force-field geometry optimization, and (iv) a second round of clustering. Packing uses a Monte-Carlo simulated annealing (MC-SA) algorithm to generate the candidate crystal structures, using maximum and minimum temperatures of $1.5 \times 10^5$ K and 300 K, respectively; heating and cooling factors of 0.025 and 0.0005, respectively; and a minimum move factor of $10^{-10}$. Clustering removes duplicate structures, which are grouped based on a radial distribution cut-off of 7.0 Å, a tolerance of 0.13, and 140 bins. A Dreiding force-field [100] geometry optimization refines the positions of the motion groups (keeping their relative atomic positions constant for each motion group) and calculates their static lattice energies. Convergence is reached after a maximum change in energy of $2 \times 10^{-5}$ kcal mol$^{-1}$, force of $10^{-3}$ kcal mol$^{-1}$ Å$^{-1}$, stress of $10^{-3}$ GPa, and atomic displacement of $10^{-5}$ Å. Candidate structures are then clustered again to remove duplicate structures. After all trials of Polymorph, a final round of clustering is performed to remove duplicate candidate structures that were generated across all trials.

#### 2.5.2. CASTEP

Plane-wave DFT-D2* [66] geometry optimizations and subsequent calculations of NMR interaction tensors are conducted in CASTEP. Two types of DFT-D2* geometry optimizations are used: truncated and convergent. Both use the RPBE functional with a plane-wave energy cut-off of 800 eV, the zeroth-order regular approximation [101] scalar-relativistic ultrasoft pseudopotentials generated on-the-fly [102], and a *k*-point spacing of 0.05 Å$^{-1}$ using the Monkhorst-Pack grid [103]. However, they differ in how they implement the LBFGS scheme [104]: truncated geometry optimizations undergo five BFGS cycles, whereas convergent geometry optimizations continue until convergence thresholds are met, which are a change in energy of $5 \times 10^{-6}$ eV atom$^{-1}$, displacement of $5 \times 10^{-4}$ Å, and force of $10^{-2}$ eV Å$^{-1}$.

Chemical shifts were calculated using the gauge including projector augmented wave [105] (GIPAW) method. The calculated $^{13}$C chemical shieldings were converted to chemical shifts using a linear regression obtained by calculating $^{13}$C chemical shielding values of structural models of *L*-histidine HCl•$H_2O$ [106], α-glycine [107], γ-glycine [108], and *L*-asparagine•$H_2O$ [109] that were refined using convergent geometry optimizations and correlating them to their previously reported experimental values (Fig. S1) [110]. Calculated $^{14}$N and $^{35}$Cl EFG tensor principal component values were converted to the MHz scale using nuclear quadrupole moments of $Q(^{14}N) = 2.04$ fm$^2$ and $Q(^{35}Cl) = -8.17$ fm$^2$ [111].

Atomic Hirshfeld charges, which are assigned in M1 and necessary for M2, were obtained from convergent geometry-optimized structural models derived from the crystal structures of α-glycinamide HCl [112], β-glycinamide HCl [113], glycine HCl [114], and alanine HCl [115] (Table S5). The sum of all Hirshfeld charges must be equal to zero; therefore, minor modifications in the value of the charges on the H and Cl atoms were made, since these have the highest standard deviations among the calculated charges.

#### 2.5.3. ShiftML2

$^{13}$C chemical shieldings were calculated using ShiftML2 [47] and converted to $^{13}$C chemical shift scale by calculating the $^{13}$C chemical shieldings on the structural models of *L*-histidine HCl•$H_2O$ [106], α-glycine [107], γ-glycine [108], and *L*-asparagine•$H_2O$ [109] that were refined with convergent geometry optimizations and correlating them to experimental $^{13}$C chemical shifts (Fig. S1) [110].

### 2.6. Metrics

QNMRX-CSP (Scheme S1) employs metrics that are derived from experimental unit cell parameters and $^{35}$Cl EFG tensors, as well as calculated static lattice energies, to identify structural models that most closely align with experimental data. These metrics use thresholds determined through extensive benchmarking calculations and blind tests on HCl salts with known crystal structures [63,64]. Four metric sets are used at different junctures in the QNMRX-CSP protocol to select the best candidate structures. See Table 2 for the combinations of metrics and thresholds used in each metric set, and **§3.3** for a description of the use of each metric set in QNMRX-CSP.

**Unit Cell Parameters**. Candidate structures are compared to the indexed unit cell parameters from PXRD as part of Metric Set 1. They are retained if their unit cell parameters are within ±20 % of the indexed unit cell parameters.

**Static Lattice Energy**. Candidate structures are retained based on their calculated static lattice energies ($E_{lat}$) and are compared to the structure with the lowest overall static lattice energy ($E_{low}$) using two approaches. The first approach, used in M2, retains candidate structures with values of $E_{lat}$ in the bottom 13.5 % of all the calculated values of $E_{lat}$, such that:

$$E_{low} \leq E_{lat} \leq 0.865 \cdot E_{low} \tag{1}$$

where $E_{low}$ is always a negative value. The second approach, used in M3, retains candidate structures with a difference in the $E_{lat}$ ($\Delta E_{lat}$) that is less than or equal to an energy threshold ($E_{thresh}$), such that:

$$\Delta E_{lat} = E_{lat} - E_{low} \leq E_{thresh} \tag{2}$$

The values of $E_{thresh}$ have been benchmarked and vary depending on the step after which each metric set is applied (Table 2).

**EFG Distance**. The EFG distance ($\Gamma_{EFG}$) is used to assess the similarity between calculated and experimental EFG tensors in the same principal axis system [66].

$$\Gamma_{EFG} = \left( \frac{1}{15} \left[ 3\Delta_{11}^2 + 3\Delta_{22}^2 + 3\Delta_{33}^2 + 2\Delta_{11}\Delta_{22} + 2\Delta_{22}\Delta_{33} + 2\Delta_{11}\Delta_{33} \right] \right)^{1/2} \tag{3}$$

$$\Delta_{kk} = \left| V_{kk}^{calc} - V_{kk}^{exp} \right| \tag{4}$$

where $V_{kk}$ ($k = 1, 2, 3$) are principal components of the calculated and experimental EFG tensors. A value of $\Gamma_{EFG} = 0$ means that the two EFG tensors are identical, whereas distinct benchmarked threshold values of $\Gamma_{EFG}$ are used for retaining structural candidates after different steps in M3 [66].

### 2.7. Structural validation

Candidate structures are validated via consideration of three parameters: the *R*-factor (*R*), the RMSD for atomic positions ($\Delta_{RMSD}$), and the reduced chi-squared ($\chi^2_{red}$) statistic, which are based on comparison of calculated and experimental PXRD, SCXRD, and multinuclear SSNMR data, respectively.

***R*-factor**. PXRD patterns were simulated in the Powder Pattern tool in Mercury 2022.3.0 with a Cu *K*α radiation source from 5° to 50°, step sizes of 0.01°, and peaks with full-width half heights of 0.1°. The comparison of any two PXRD patterns was performed using the following equation:

$$R = \frac{\sum |(|F_0| - |F_c|)|}{\sum |F_0|} \times 100\ \% \quad (5)$$

$F_0$ and $F_c$ are the calculated signal amplitudes of the reference and candidate structures, respectively. According to the CSD, a $R \leq 10$ % indicates that the structural model agrees with the PXRD pattern [116, 117].

**Atomic position RMSDs**. Values of $\Delta_{RMSD}$ were calculated in the CSD-Materials Crystal Packing Similarity module in Mercury 2022.3.0 using a 15-molecule cluster and distance and angle tolerances of 20 % and 20°, respectively. In comparing two crystal structures, a $\Delta_{RMSD} \leq$ 0.2 Å indicates that the two structures have similar packing motifs and are considered a good structural match [11].

**Reduced-χ** [2]. The agreement between experimental and calculated NMR interactions is assessed using the $\chi^2_{red}$ statistic [78]:

$$\chi^2_{red} = \frac{1}{n-f} \sum_{i=1}^{n} \frac{\left(X_i^M - X_i^E\right)^2}{\sigma_i^2} \quad (6)$$

where $X_i^M$ and $X_i^E$ are the calculated and experimental NMR parameters, respectively, σ is the benchmarked variance between them, *n* is the number of observations, and *f* is an optional value for the number of adjustable model parameters (herein, *f* is set to zero).

A value of $\chi^2_{red} \leq 1$ indicates a good candidate structure, whereas significantly higher values indicate poorer agreement, and values close to zero indicate overfitting. Three sets of NMR data were used for calculating $\chi^2_{red}$ values, including $^{13}$C chemical shifts (from GIPAW and ShiftML2), $^{14}$N EFG tensors, and $^{35}$Cl EFG tensors. The benchmarked variances in the $^{13}$C chemical shift calculations were $\sigma^{CS}(^{13}C) = 3.1$ and 4.93 ppm for GIPAW [118] and ShiftML2 [47], respectively, and for EFG tensor principal components $\sigma^{EFG}(^{14}N) = 0.031$ a.u. and $\sigma^{EFG}(^{35}Cl) = 0.011$ a.u [66].

## 3. Results and discussion

QNMRX-CSP, which uses a combination of PXRD and SSNMR data, along with MC-SA routines and dispersion corrected DFT-D2* calculations, was employed for the *de novo* crystal structure determination of *L*-Ala-$NH_2$. A powder sample of *L*-Ala-$NH_2$ was characterized by both PXRD (**§3.1**) and $^{35}$Cl SSNMR (**§3.2**). The indexing of the PXRD pattern and the extraction of the $^{35}$Cl EFG tensors from the $^{35}$Cl SSNMR spectra allowed us to determine the crystal structure of *L*-Ala-$NH_2$ *de novo* using QNMRX-CSP (**§3.3**). Multinuclear SSNMR ($^{13}$C, $^{14}$N, and $^{35}$Cl) data and an independent determination of the crystal structure using SCXRD data were used to validate the best structural model (**§3.4**).

### 3.1. X-ray diffraction

A PXRD pattern (Fig. 1A) was acquired from a microcrystalline powder sample of *L*-Ala-$NH_2$ for QNMRX-CSP analysis. This was indexed to obtain the space group (monoclinic $P2_1$, Group 4) and unit cell parameters (Table 1). It is emphasized that the indexing of the PXRD patterns relies mainly upon accurate fitting of the 2θ values; the reader is cautioned about the use of peak intensities for such purposes, since they can be influenced by numerous factors, including instrumentation set-up, systematic errors, and preferred orientations in crystalline samples [119–121].

The crystal structure of *L*-Ala-$NH_2$ was determined independently using SCXRD data (Table S1), for purposes of validation; since QNMRX-CSP is used for *de novo* structural determination, the SCXRD structure was not revealed until the final stages of validation (*i.e.*, one of the co-authors, Dr. Xinsong Lin, did not share the structure until this point). The crystal structure is available from the CSD under deposition number 2432183.

There is good agreement between the simulated PXRD pattern based on the SCXRD structure and that from the DFT-D2* geometry-optimized SCXRD structure (hereafter referred to as the SCXRD* structure, Fig. 1B and C). The remainder of the PXRD patterns in Fig. 1 are discussed in **§3.3** and **§3.4**.

### 3.2. Solid-state NMR spectroscopy

**$^{35}$Cl{$^1$H} NMR spectra**. The $^{35}$Cl{$^1$H} SSNMR spectra of *L*-Ala-$NH_2$ were acquired under static and MAS conditions at two fields. The spectra feature central transition (CT, $+1/2 \leftrightarrow -1/2$) powder patterns that are influenced by second-order quadrupolar and chemical shift anisotropy interactions, with no indication of any impurity phases (Fig. 2). These spectra were simulated using a single set of $^{35}$Cl EFG tensors, chemical shift tensors, and Euler angles (Table 3). Based on our previous observations, the small magnitude of $C_Q$ and high value of $\eta_Q$ indicate a $Cl^-$ ion environment featuring multiple hydrogen bonds (*i.e.*, *r*(H···Cl) < 2.6 Å) [122], and no short contacts (*r*(H···Cl) ≲ 2.2 Å) [123–126].

**$^{14}$N{$^1$H} NMR spectra**. The ultra-wideline $^{14}$N{$^1$H} SSNMR spectrum of *L*-Ala-$NH_2$ (Fig. 3) was acquired using the WURST-CPMG pulse sequence and stepping the transmitter across the breadth of the pattern. A first-order Pake-like doublet is observed that is assigned to the $RNH_3^+$ group. The signal-to-noise ratio for this pattern is not high due to a short effective $T_2$ time constant ($T_2^{eff}$) and the need to acquire 5 sub-spectra at different transmitter offsets (each sub-spectrum required *ca.* 2.3 h of acquisition time). Accordingly, the "feet" of the $RNH_3^+$ pattern are not observed. Furthermore, there is no $^{14}$N powder pattern corresponding to the amide moiety, due to its large quadrupolar coupling constant and concomitantly broad first-order powder pattern (from the theoretical prediction below, if $C_Q(^{14}N) = -2.902$ MHz, then the Pake-like doublet will have a width of *ca.* 4.35 MHz). Additionally, the $T_2^{eff}$ is expected to be very short in comparison to that of the $RNH_3^+$ nitrogen. A possible future avenue to determine the experimental $^{14}$N SSNMR of the amide moiety would be using $^{14}$N–$^1$H heteronuclear multiple-quantum coherence [127,128]. Nonetheless, the experimental spectrum was fit with a single $^{14}$N pattern, yielding $^{14}$N EFG tensor parameters listed in Table 4. Based on previous observations, the small magnitude of $C_Q$ and $\eta_Q$ value near zero indicates a pseudotetrahedral $RNH_3^+$ moeity [129]; this is consistent with the absence of short H···Cl contacts.

**$^1$H→$^{13}$C{$^1$H} NMR spectrum**. The $^1$H→$^{13}$C{$^1$H} CP/MAS NMR spectra of *L*-Ala-$NH_2$ reveal three distinct $^{13}$C chemical shifts (Fig. 4), each assigned to unique crystallographic carbon sites (Table 4) and consistent with $Z' = 1$. No additional peaks or features are present, indicating the absence of any impurity phase. Assignments of the $^{13}$C chemical shifts are provided in the figure. The peak corresponding to $C_2$ is likely broadened due to $^{14}$N-$^{13}$C residual dipolar coupling [130].

**SSNMR data and structural interpretation**. Detailed discussions regarding structural interpretations of the *L*-Ala-$NH_2$ structure based on the $^{35}$Cl and $^{14}$N SSNMR data are in **§3.5**.

### 3.3. QNMRX-CSP of L-Ala-$NH_2$

QNMRX-CSP was applied to *L*-Ala-$NH_2$ using the space group and unit cell parameters determined from indexing the PXRD pattern (Table 1), as well as the $^{35}$Cl EFG tensors (Table 3). Progression through

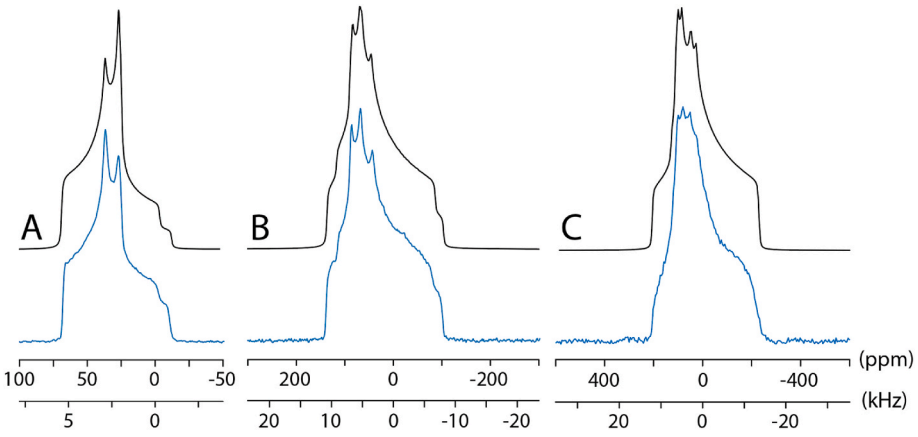


**Fig. 2.** $^{35}$Cl{$^{1}$H} Hahn-echo NMR spectra of *L*-Ala-$NH_2$ (blue) acquired at 18.8 T under (A) MAS and (B) static conditions, as well as at 14.1 T (C) under static conditions. Spectral simulations (black) are provided for each of these spectra using the parameters in Table 3. (For interpretation of the references to colour in this figure legend, the reader is referred to the Web version of this article.)

**Table 3**
Experimental and calculated$^{35}$Cl EFG and chemical shift tensors.[a-e]

| | | $C_Q$ (MHz) | $\eta_Q$ | $\delta_{iso}$ (ppm) | Ω (ppm) | κ | α (°) | β (°) | γ (°) |
|---|---|---|---|---|---|---|---|---|---|
| *L*-Ala-$NH_2$ | Exp. | 2.71(2) | 0.75(3) | 69.6(3) | 64(3) | −0.35(5) | 213(10) | 82(3) | 5(5) |
| 12-72 | Calc. | 2.404 | 0.93 | 66.8 | 55.5 | −0.17 | 218 | 76 | 2 |
| 12-72* | Calc. | 2.438 | 0.85 | 65.6 | 56.0 | −0.16 | 217 | 75 | 2 |
| 6-440 | Calc. | −1.82 | 0.74 | 72.4 | 30.4 | 0.22 | 30 | 66 | 164 |
| 1-536 | Calc. | 1.408 | 0.29 | 48.0 | 85.2 | 0.61 | 6 | 58 | 149 |
| 8-388 | Calc. | −4.713 | 0.74 | 55.6 | 67.6 | 0.36 | 75 | 64 | 90 |
| SCXRD[f] | Calc. | 1.669 | 0.79 | 29.7 | 39.0 | 0.79 | 224 | 67 | 345 |
| SCXRD*[g] | Calc. | 2.457 | 0.88 | 65.3 | 56.3 | −0.17 | 218 | 76 | 2 |

[a] The principal components of the EFG tensors are defined such that $|V_{33}| \geq |V_{22}| \geq |V_{11}|$. The quadrupolar coupling constant and asymmetry parameter are given by $C_Q = eQ(V_{33})/h$, and $\eta_Q = (V_{11} - V_{22})/V_{33}$, respectively. The sign of $C_Q$ cannot be determined from the experimental $^{35}$Cl spectra.
[b] The principal components of the chemical shift tensors are defined using the frequency-ordered convention, with $\delta_{11} \geq \delta_{22} \geq \delta_{33}$. The isotropic chemical shift, span, and skew are given by $\delta_{iso} = (\delta_{11} + \delta_{22} + \delta_{33})/3$, $\Omega = \delta_{11} - \delta_{33}$, and $\kappa = 3(\delta_{22} - \delta_{iso})/\Omega$, respectively.
[c] The Euler angles α, β, and γ define the relative orientation of the EFG and chemical shift tensors using the *ZY'Z*" convention for rotation.
[d] $^{35}$Cl chemical shielding values were converted to the chemical shift scale using the experimental chemical shift of *L*-histidine HCl·$H_2O$ set to 34.5 ppm and refining the structure from CSD (HISTCM01) with DFT-D2* and calculating the $^{35}$Cl chemical shielding [1].
[e] The experimental uncertainties in the last digit for each value are indicated in parentheses.
[f] $^{35}$Cl NMR parameters were calculated using the structure determined from SCXRD.
[g] $^{35}$Cl NMR parameters were calculated using the DFT-D2* geometry-optimized SCXRD structure.

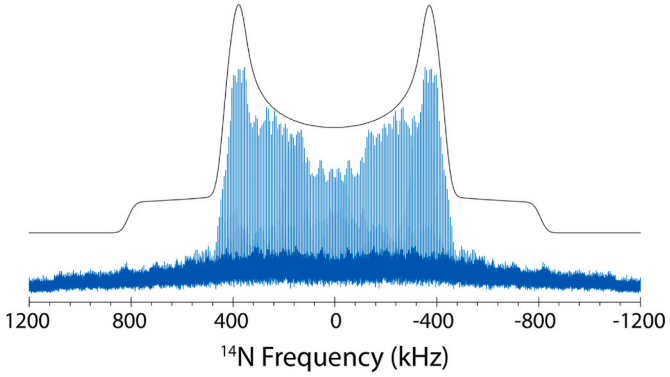


**Fig. 3.** $^{14}$N{$^{1}$H} VOCS WURST-CPMG NMR spectra of *L*-Ala-$NH_2$ acquired at 18.8 T under static conditions. A spectral simulation is shown in black.

the three modules is described below and tracked in Scheme S1 and Table 5. All metric sets used to retain candidate structures are provided in Table 2.

**Module 1**. M1 consists of four steps. M1 step 1: the *L*-Ala-$NH_2$ organic cation was built in Materials Studio. M2 step 2: a convergent geometry optimization was performed on the cation in a *P*1 15 × 15 × 15 Å$^3$ unit cell. M1 step 3: a $Cl^-$ ion was added to the asymmetric unit and atomic Hirshfeld charges were assigned. M1 step 4, the cation and $Cl^-$ ion were assigned as independent motion groups.

**Module 2**. In M2, Polymorph (**§2.5.1**) was performed for 20 trials, generating 89,247 candidate structures. Metric Set 1 was applied, retaining 612 candidate structures.

**Module 3**. In M3, steps 1, 2, and 3 involve (1) truncated geometry optimization, (2) convergent geometry optimization, and (3) unit cell adjustment to the experimental values (from PXRD data) followed by a second convergent geometry optimization. For each step, $^{35}$Cl EFG tensors were calculated following the geometry optimization. Application of Metric Sets 2, 3, and 4 (Table 2) retained 79, 50, and 0 structures for each step, respectively (Table 5).

To better understand why no suitable structural models emerged, we reevaluated the 50 candidate structures that were discarded using Metric Set 4. First, only three unique structural motifs were identified: Structural model 6–440, which has the lowest $\Gamma_{EFG}$ and $E_{lat}$, is representative of 46 of the 50 candidate structures (via observation of their similar RMSD values). The two remaining structural motifs, structures 1–536 and 8–388 (ranked in increasing order of energy), represent 2 of the remaining 4 structures. Second, comparison of the simulated PXRD patterns of these three structural motifs (Fig. 1D–F) to the experimental PXRD pattern revealed a reasonable match only for 8–388; however, there are additional peaks and some mismatches in peak intensities.

**Table 4**
Experimental and calculated $^{14}$N EFG tensor parameters and $^{13}$C chemical shifts.[a]

| | | $C_Q(^{14}N)$ (MHz)[b] | $\eta_Q(^{14}N)$[b] | $\delta_{iso}$(C1) (ppm)[c] | $\delta_{iso}$(C2) (ppm)[c] | $\delta_{iso}$(C3) (ppm)[c] |
|---|---|---|---|---|---|---|
| *L*-Ala-$NH_2$ | Exp. | 1.08(3) | 0.08(2) | 17.5(4) | 49.4(2.0) | 175.2(5) |
| 12-72 | Calc. | 1.239 | 0.06 | 13.2/10.7[d] | 50.4/47.5 | 175.0/179.0 |
| 12-72* | Calc. | 1.234 | 0.05 | 13.2/10.8 | 50.4/47.5 | 174.9/178.9 |
| 6-440 | Calc. | 1.487 | 0.22 | 14.2/10.3 | 51.4/43.2 | 172.1/177.0 |
| 1-536 | Calc. | 1.540 | 0.13 | 11.8/7.5 | 52.1/43.5 | 173.5/173.5 |
| 8-388 | Calc. | 1.203 | 0.10 | 18.5/12.7 | 54.9/48.6 | 170.4/175.0 |
| SCXRD | Calc. | 1.665 | 0.08 | 0.5/−0.9 | 47.1/41.1 | 177.7/183.7 |
| SCXRD* | Calc. | 1.227[e] | 0.05[e] | 13.2/10.7 | 50.4/47.4 | 175.0/178.9 |

[a] The experimental uncertainties in the last digit for each value are indicated in parentheses.
[b] The sign of $C_Q$ cannot be determined from the experimental $^{14}$N spectra. The calculated $^{14}$N EFG tensors were obtained from plane-wave DFT calculations. Definitions of quadrupolar and EFG tensor parameters are given in Table 2.
[c] Assignments of the $^{13}$C chemical shifts to *L*-Ala-$NH_2$ are provided in Fig. 4.
[d] $^{13}$C chemical shielding values were calculated using GIPAW (left) and ShiftML2 (right) and converted to the chemical shift scale, as described in Fig. S1.
[e] The $^{14}$N EFG tensors of the amide moiety were calculated using GIPAW, yielding $C_Q(^{14}N) = -2.902$ MHz and $\eta_Q(^{14}N) = 0.27$.

Furthermore, 8–388 has the highest values of $\Gamma_{EFG}$ and $E_{lat}$, making it less convincing as a structural match (Table 6).

This led us to reexamine the 29 structures discarded with Metric Set 3 (Table 5). All but one structural model was eliminated due to high $\Gamma_{EFG}$ values. The remaining model, 12–72, has a structure distinct from that of the three aforementioned motifs, with $\Gamma_{EFG} = 0.222$ MHz and $\Delta E_{lat} = 60.52$ kJ mol$^{-1}$, the latter of which led to its removal. As such, $E_{thresh}$ was adjusted to 60.52 kJ mol$^{-1}$ in Metric Set 3. After subjecting 12–72 to M3 step 3, it was found to have the lowest $\Gamma_{EFG}$ and $E_{lat}$ (Table 6), allowing it to be retained with Metric Set 4, and having a simulated PXRD pattern that matches best with the experimental pattern (Fig. 1G). Given that Metric Set 3 had to be adjusted, we decided to take further steps to validate the structure of 12–72.

### 3.4. Validation of the structure for L-Ala-$NH_2$

Several steps were taken to validate the final four structural models obtained from QNMRX-CSP (as ranked by $\Gamma_{EFG}$ and $E_{lat}$), including: (i) *R*-factors calculated from comparison of experimental and simulated PXRD patterns (these can sometimes be unreliable) [131,132]; (ii) $\Delta_{RMSD}$s of atomic positions (this requires a known crystal structure); and (iii) $\chi^2_{red}$ values obtained from comparison of sets of multinuclear SSNMR data. For instance, $^{13}$C and $^{14}$N SSNMR spectra of *L*-Ala-$NH_2$ can aid in validating the candidate structures.

$\chi^2_{red}$ values (Table 7) were calculated using only the $^{13}$C chemical shifts (both from GIPAW and ShiftML2, Table 4), $^{14}$N EFG tensors, or $^{35}$Cl EFG tensors (from DFT, Tables 3 and 4), all pairwise combinations of these parameters, and the combination of all three sets. A survey of the $\chi^2_{red}$ values obtained from GIPAW and ShiftML2 (left and right numbers in each column of Table 7, respectively) reveals that the $\chi^2_{red}$ values featuring $^{35}$Cl EFG tensors alone or in combination with other NMR parameters are lowest for 12–72, which is the only structural model having a simulated PXRD pattern matching that from experiment. This supports the value of measurement and calculation of $^{35}$Cl EFG tensors for QNMRX-CSP applications and emphasizes the importance of including other NMR-based metrics for structural validation and

**Table 5**
The initial and final numbers of candidate structures retained by applications of metric sets in QNMRX-CSP.

| Original Metric Set | Initial | | Retained |
|---|---|---|---|
| 1 | 89247 | → | 612 |
| 2 | 612 | → | 79 |
| 3 | 79 | → | 50 |
| 4 | 50 | → | 0 |
| Adjusted Metric Set | | | |
| 1 | 89247 | → | 612 |
| 2 | 612 | → | 79 |
| 3 | 79 | → | 51 |
| 4 | 51 | → | 1 |

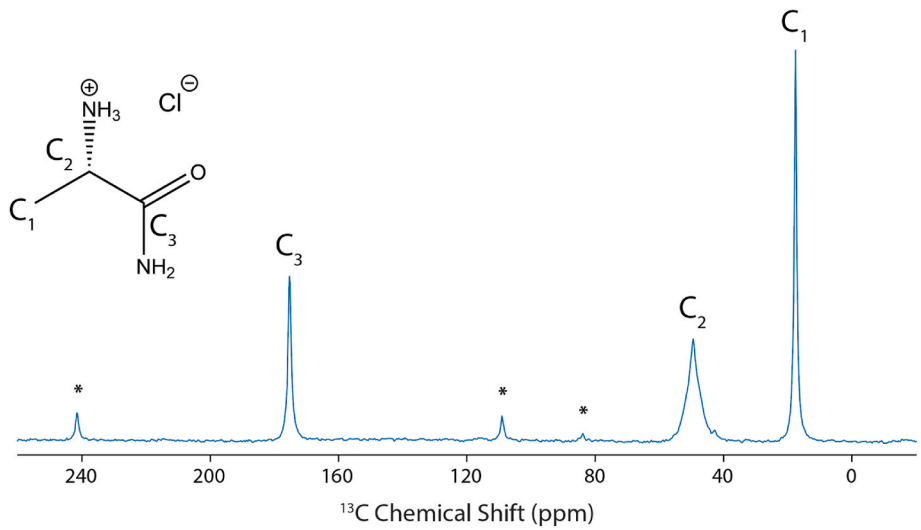


**Fig. 4.** $^1$H→$^{13}$C{$^1$H} CP/MAS NMR spectra of *L*-Ala-$NH_2$ acquired at 14.1 T with a spinning rate of $\nu_{rot} = 10$ kHz. Spinning side bands are indicated by asterisks. Peak assignments are indicated in the molecular inset (upper left).

**Table 6**
Structural validation of the candidate structures for *L*-Ala-$NH_2$ from QNMRX-CSP.

| | $\Gamma_{EFG}$ (MHz) | $\Delta E_{lat}$ (kJ/mol)[a] | $\Delta_{RMSD}$ (Å)[b] | *R* (%)[c] |
|---|---|---|---|---|
| 12-72 | 0.216 | 0.000 | 0.073/0.049/0.001 | 125.57/44.42/3.69 |
| 6-440 | 0.633 | 44.53 | 0.542/0.545/0.559 | 98.91/126.52/119.77 |
| 1-536 | 0.983 | 52.59 | 0.718/0.724/0.735 | 94.46/118.52/113.49 |
| 8-388 | 1.419 | 84.26 | 0.723/0.702/0.704 | 136.75/64.84/61.45 |

[a] The static lattice energy difference ($\Delta E_{lat}$) between the four structural models from QNMRX-CSP, normalized such that the lowest energy structure is $E_{lat} = 0$ kJ $mol^{-1}$.

[b] $\Delta_{RMSD}$ values are calculated by comparing the QNMRX-CSP structural model to the SCXRD structure (left), and to the SCXRD* structure (middle). The QNMRX-CSP structures had their unit cell parameters adjusted to match the SCXRD determined ones and underwent DFT-D2* geometry optimizations. The $\Delta_{RMSD}$ values of those structures were calculated by comparing them to the SCXRD* structure (right).

[c] *R* values were calculated using the simulated PXRD patterns for the structural models from QNMRX-CSP compared to the experimental PXRD pattern (left) and simulated PXRD pattern of SCXRD* (middle). Moreover, *R* values were calculated using the simulated PXRD patterns of the structural models, with unit cell parameters adjusted to match the SCXRD determined ones, and after a DFT-D2* geometry optimization, were compared to the simulated PXRD pattern of SCXRD* (right).

**Table 7**
$\chi^2_{red}$ values for the candidate structures of *L*-Ala-$NH_2$ from QNMRX-CSP. [a,b]

| | $^{13}C$ | $^{14}N$ | $^{35}Cl$ | $^{13}C + ^{14}N$ | $^{13}C + ^{35}Cl$ | $^{14}N + ^{35}Cl$ | $^{13}C + ^{14}N + ^{35}Cl$ |
|---|---|---|---|---|---|---|---|
| 12-72 | ***0.72*/0.87** | **0.56** | ***1.21*** | ***0.64*/0.71** | ***0.96*/1.04** | ***0.88*** | ***0.83*/0.88** |
| 6-440 | **0.91/1.28** | 4.16 | 9.68 | 2.54/2.72 | 5.30/5.48 | 6.92 | 4.92/5.04 |
| 1-536 | 1.56/1.89 | 4.85 | 28.84 | 3.21/3.37 | 15.20/15.37 | 16.84 | 11.75/11.86 |
| 8-388 | 2.00/***0.33*** | ***0.34*** | 52.83 | **1.17/*0.34*** | 27.42/26.58 | 26.59 | 18.39/17.84 |

[a] In each column, the lowest $\chi^2_{red}$ values are italicized, and those in bold agree well with experiment, as indicated by a value $\lesssim 1$.

[b] The values on the left and right in each column are obtained from DFT and ShiftML2 calculations, respectively.

perhaps even further structural refinement — this is crucial because numerous candidate structures can have calculated NMR parameters that agree with a single (or, in some cases, multiple) experimental NMR parameters.

The most convincing method of validating a candidate structure from QNMRX-CSP is a comparison to a SCXRD structure, or preferably, a structural model based on a dispersion-corrected DFT geometry optimization of the SCXRD structure. The reason for this is two-fold: (i) the hydrogen atom positions are most often not well-defined in SCXRD structures [72,133,134] and (ii) the NMR interaction tensors,

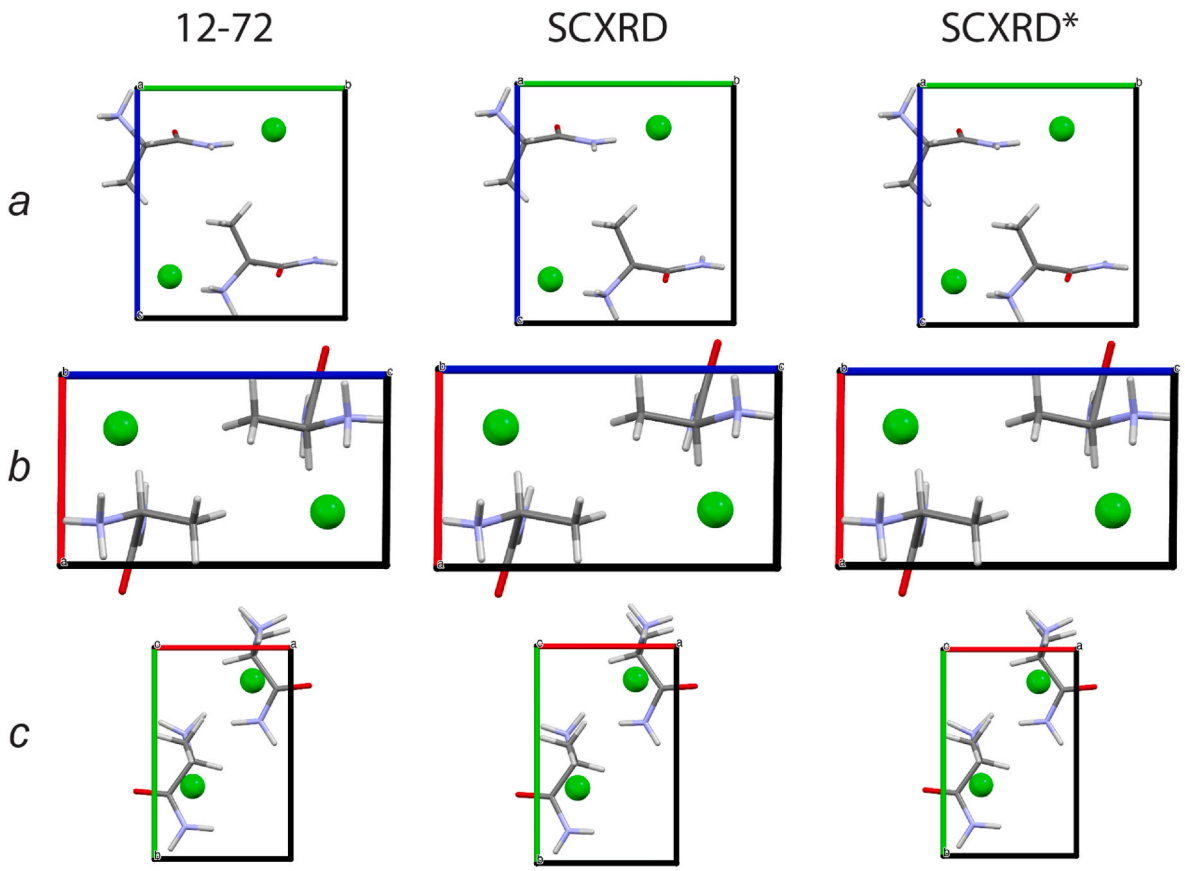


**Fig. 5.** A view along each crystallographic axis (*a*, *b*, and *c*) of *L*-Ala-$NH_2$, as determined by QNMRX-CSP (left), SCXRD (middle), and SCXRD* (right).

particularly EFG tensors, are extremely sensitive to the positions of hydrogen atoms [65,66,135], especially in crystals of organic molecules, where weak interactions like hydrogen bonding, π-π stacking, and other van der Waals forces are major determinants of structure and packing.

This motivated us to grow a single crystal of *L*-Ala-$NH_2$, from which we determined a crystal structure using SCXRD (Table S1) and to use this as a starting point for a geometry optimization using DFT-D2* (*i.e.*, SCXRD* models), with subsequent calculations of NMR interaction tensors for both (Tables 3 and 4). A visual comparison of 12–72 and either the SCXRD or SCXRD* structures provisionally confirms that 12–72 is a good match (Fig. 5); this is quantitatively confirmed by calculating the $\Delta_{RMSD}$ values, where that of the SCXRD* structure is slightly superior (Table 6).

The *R*-factors are another matter. Simulated PXRD patterns generated from the 12–72 structural model yield *R* values of 125.57 and 44.42 from comparisons to the experimental PXRD and simulated PXRD (from SCXRD*) patterns, respectively, indicating poor quantitative matches (Table 6). Comparison of the unit cell parameters obtained from indexing of the PXRD pattern and SCXRD structure reveal subtle differences in *a*, *b*, *c*, and β (Table 1). Hence, we adjusted the unit cell parameters to those obtained from the latter, conducted a DFT-D2* geometry optimization, and calculated the NMR interaction tensors. The resulting structural model, which we refer to as 12–72*, has a better RMSD and a dramatically improved *R*-factor (Table 6), with excellent quantitative agreement between the experimental and simulated PXRD patterns (Fig. 1H). Furthermore, there is a significant improvement in agreement between the experimental and calculated $^{35}$Cl NMR interaction tensors, and minimal changes in the $^{13}$C and $^{14}$N NMR interaction tensors (Tables 3 and 4). The use of the SCXRD structure for validating the structure of *L*-Ala-$NH_2$ highlights the importance of obtaining accurate unit cell parameters for use in QNMRX-CSP – the collection of PXRD data in transmission mode and/or with synchrotron X-ray sources is clearly of great benefit in this respect.

### 3.5. Discussion on the structure of L-Ala-$NH_2$

Since the *de novo* structural model of *L*-Ala-$NH_2$ is in good agreement with the known crystal structure, it is possible to investigate relationships between the $^{35}$Cl and $^{14}$N EFG tensors and hydrogen bonding environments. The $Cl^-$ ion environment is found to be consistent with the predictions made solely from the $^{35}$Cl EFG tensors (**§3.2**). The $Cl^-$ ion environment features four H···Cl hydrogen bonds and no short contacts (at least by the definition of $r$(H···Cl) $\lesssim$ 2.2 Å). However, there are similar $r$(H···Cl) contacts of 2.211 and 2.213 Å and one longer one of 2.257 Å, all involving $RNH_3$ groups (Fig. S2). The $^{35}$Cl EFG tensor components are oriented near (but not exactly colinear with) the directions of the H···Cl hydrogen bonds, with $V_{11}$, $V_{22}$, and $V_{33}$ near the shortest (2.211 Å), third shortest (2.257 Å), and second shortest (2.213 Å), respectively, which is consistent with previous studies relating the $^{35}$Cl EFG tensor principal components to structural features around the $Cl^-$ ion [123,129].

The $RNH_3^+$ moiety features a N in a pseudotetrahedral environment (Fig. S2), and as mentioned above, all three H atoms participate in H···Cl hydrogen bonds with lengths ranging from 2.213 to 2.257 Å. The small magnitude of $C_Q(^{14}N)$ (1.08 MHz) and a $^{14}$N EFG tensor of near-axial symmetry ($\eta_Q = 0.08$) are consistent with the absence of short H···Cl contacts and the presence of three or more longer contacts, aligning with predictions in **§3.2** and previous studies.

## 4. Conclusions

Herein, a *de novo* crystal structure determination using QNMRX-CSP has been demonstrated for the first time. With *L*-Ala-$NH_2$ as the target compound, it was shown that knowledge of the unit cell parameters, space group, and $^{35}$Cl EFG tensors was sufficient to determine the structure. To increase our confidence in the structural determination, we validated the most probable candidate structure using $\chi^2_{red}$ values derived from combinations of $^{13}$C chemical shifts and $^{14}$N and $^{35}$Cl EFG tensors, and made further validation checks against a new SCXRD structure, as well as a related DFT-dispersion corrected geometry-optimized structural model. This approach demonstrates the effectiveness of combining multinuclear SSNMR data for validating candidate structures, and suggests possible use for structural determination of organic solids of increasing complexity.

As QNMRX-CSP is still a nascent protocol, the *de novo* crystal structure determination of *L*-Ala-$NH_2$ has revealed some limitations that we hope to address. First, further benchmarking studies are needed to determine more robust threshold values for metrics like $E_{lat}$. Second, accurate unit cell parameters are necessary to obtain structural models that represent the most probable crystal structure, as reckoned via comparisons of experimental and calculated $^{35}$Cl EFG tensors and PXRD patterns. The results presented herein suggest promise for the investigation of increasingly complex systems, as well as new avenues of exploration. For instance, QNMRX-CSP should work very well in combination with Rietveld refinement methods, with each technique providing key information for the other, which may lead to increases in their efficiency and reliability. In addition, new dispersion-correction methods (*e.g.*, DFT-D3, DFT-D4, DFT-D3-BJ) [136–138] may allow us to design new QNMRX-CSP protocols employing geometry optimizations that adjust both the atomic positions and unit cell parameters, which may reduce reliance on having accurate crystallographic parameters, and perhaps expand these methods to a wider range of solids.

## Declaration of competing interest

There are no conflicts to declare.

## Acknowledgments

R.W.S. is grateful for research support from The Florida State University and the National High Magnetic Field Laboratory (NHMFL), which is funded by the National Science Foundation Cooperative Agreement (DMR-2128556) and by the State of Florida. This work was supported in part by the U.S. Department of Energy, Office of Science, Office of Basic Energy Sciences, under Award Number DE-SC0022310, covering expenses related to development of computational protocols and associated postdoctoral wages.

## Appendix A. Supplementary data

Supplementary data to this article can be found online at https://doi.org/10.1016/j.ssnmr.2025.102034.

## Data availability

Data will be made available on request.

## References

[1] C.R. Groom, I.J. Bruno, M.P. Lightfoot, S.C. Ward, The Cambridge structural database, Acta Crystallogr B Struct Sci Cryst Eng Mater 72 (2) (2016) 171–179, https://doi.org/10.1107/S2052520616003954.
[2] R. Taylor, P.A.A. Wood, Million crystal structures: the whole is greater than the sum of its parts, Chem. Rev. 119 (16) (2019) 9427–9477, https://doi.org/10.1021/acs.chemrev.9b00155.
[3] T. Friščić, C. Mottillo, H.M. Titi, Mechanochemistry for synthesis, Angew. Chem. Int. Ed. 59 (3) (2020) 1018–1029, https://doi.org/10.1002/anie.201906755.
[4] K.D.M. Harris, M. Tremayne, B.M. Kariuki, Contemporary advances in the use of powder X-Ray diffraction for structure determination, Angew. Chem. Int. Ed. 40 (9) (2001) 1626–1651, https://doi.org/10.1002/1521-3773(20010504)40:9<1626::AID-ANIE16260>3.0.CO;2-7.
[5] K.D.M. Harris, E.Y. Cheung, How to determine structures when single crystals cannot be grown: opportunities for structure determination of molecular materials using powder diffraction data, Chem. Soc. Rev. 33 (8) (2004) 526, https://doi.org/10.1039/b409059b.

[6] J.P.M. Lommerse, W.D.S. Motherwell, H.L. Ammon, J.D. Dunitz, A. Gavezzotti, D. W.M. Hofmann, F.J.J. Leusen, W.T.M. Mooij, S.L. Price, B. Schweizer, et al., A test of crystal structure prediction of small organic molecules, Acta Crystallogr. B 56 (4) (2000) 697–714, https://doi.org/10.1107/S0108768100004584.

[7] W.D.S. Motherwell, H.L. Ammon, J.D. Dunitz, A. Dzyabchenko, P. Erk, A. Gavezzotti, D.W.M. Hofmann, F.J.J. Leusen, J.P.M. Lommerse, W.T.M. Mooij, et al., Crystal structure prediction of small organic molecules: a second blind test, Acta Crystallogr. B 58 (4) (2002) 647–661, https://doi.org/10.1107/S0108768102005669.

[8] G.M. Day, W.D.S. Motherwell, H.L. Ammon, S.X.M. Boerrigter, R.G. Della Valle, E. Venuti, A. Dzyabchenko, J.D. Dunitz, B. Schweizer, B.P. Van Eijck, et al., A third blind test of crystal structure prediction, Acta Crystallogr. B 61 (5) (2005) 511–527, https://doi.org/10.1107/S0108768105016563.

[9] G.M. Day, T.G. Cooper, A.J. Cruz-Cabeza, K.E. Hejczyk, H.L. Ammon, S.X. M. Boerrigter, J.S. Tan, R.G. Della Valle, E. Venuti, J. Jose, et al., Significant progress in predicting the crystal structures of small organic molecules - a report on the fourth blind test, Acta Crystallogr. B 65 (2) (2009) 107–125, https://doi.org/10.1107/S0108768109004066.

[10] D.A. Bardwell, C.S. Adjiman, Y.A. Arnautova, E. Bartashevich, S.X.M. Boerrigter, D.E. Braun, A.J. Cruz-Cabeza, G.M. Day, R.G. Della Valle, G.R. Desiraju, et al., Towards crystal structure prediction of complex organic compounds - a report on the fifth blind test, Acta Crystallogr. B 67 (6) (2011) 535–551, https://doi.org/10.1107/S0108768111042868.

[11] A.M. Reilly, R.I. Cooper, C.S. Adjiman, S. Bhattacharya, A.D. Boese, J. G. Brandenburg, P.J. Bygrave, R. Bylsma, J.E. Campbell, R. Car, et al., Report on the sixth blind test of organic crystal structure prediction methods, Acta Crystallogr B Struct Sci Cryst Eng Mater 72 (4) (2016) 439–459, https://doi.org/10.1107/S2052520616007447.

[12] L.M. Hunnisett, J. Nyman, N. Francia, N.S. Abraham, C.S. Adjiman, S. Aitipamula, T. Alkhidir, M. Almehairbi, A. Anelli, D.M. Anstine, et al., The seventh blind test of crystal structure prediction: structure generation methods, Acta Crystallogr. B 80 (6) (2024) 517–547, https://doi.org/10.1107/S2052520624007492.

[13] K.S. Gushurst, J. Nyman, S.X.M. Boerrigter, The PO13 crystal structure of ROY, CrystEngComm 21 (9) (2019) 1363–1368, https://doi.org/10.1039/c8ce01930d.

[14] H.R. Karfunkel, Z.J. Wu, A. Burkhard, G. Rihs, D. Sinnreich, H.M. Buerger, J. Stanek, Crystal packing calculations and rietveld refinement in elucidating the crystal structures of two modifications of 4-Amidinoindanone guanylhydrazone, Acta Crystallogr. B 52 (3) (1996) 555–561, https://doi.org/10.1107/S0108768195017174.

[15] N. Panina, F.J.J. Leusen, F.F.B.J. Janssen, P. Verwer, H. Meekes, E. Vlieg, G. Deroover, Crystal structure prediction of organic pigments: quinacridone as an example, J. Appl. Crystallogr. 40 (1) (2007) 105–114, https://doi.org/10.1107/S0021889806043767.

[16] M.A. Neumann, C. Tedesco, S. Destri, D.R. Ferro, W. Porzio, Bridging the gap – structure determination of the red polymorph of tetrahexylsexithiophene by Monte Carlo simulated Annealing, first-principles DFT calculations and rietveld refinement, J. Appl. Crystallogr. 35 (3) (2002) 296–303, https://doi.org/10.1107/S0021889802002844.

[17] C. Graiff, D. Pontiroli, L. Bergamonti, C. Cavallari, P.P. Lottici, G. Predieri, Structural investigation of N,N′-Methylenebisacryl amide via X-Ray diffraction assisted by crystal structure prediction, J. Appl. Crystallogr. 48 (2015) 550–557, https://doi.org/10.1107/S1600576715004161.

[18] R. Caputo, S. Demir, A. Tekin, First-principles crystal structure prediction of Cu (I)-TCNQ polymorphs, J. Phys. Chem. C 124 (1) (2020) 70–82, https://doi.org/10.1021/acs.jpcc.9b09007.

[19] J.D. Gale, GULP: a computer program for the symmetry-adapted simulation of solids, J. Chem. Soc., Faraday Trans. 93 (4) (1997) 629–637, https://doi.org/10.1039/a606455h.

[20] C.W. Glass, A.R. Oganov, N. Hansen, USPEX—Evolutionary crystal structure prediction, Comput. Phys. Commun. 175 (11–12) (2006) 713–720, https://doi.org/10.1016/j.cpc.2006.07.020.

[21] D.C. Lonie, E. Zurek, XtalOpt: an open-source evolutionary algorithm for crystal structure prediction, Comput. Phys. Commun. 182 (2) (2011) 372–387, https://doi.org/10.1016/j.cpc.2010.07.048.

[22] C.J. Pickard, R.J. Needs, *Ab initio* random structure searching, J. Phys. Condens. Matter 23 (5) (2011) 053201, https://doi.org/10.1088/0953-8984/23/5/053201.

[23] Y. Wang, J. Lv, L. Zhu, Y. Ma, CALYPSO: a method for crystal structure prediction, Comput. Phys. Commun. 183 (10) (2012) 2063–2070, https://doi.org/10.1016/j.cpc.2012.05.008.

[24] T. Yamashita, S. Kanehira, N. Sato, H. Kino, K. Terayama, H. Sawahata, T. Sato, F. Utsuno, K. Tsuda, T. Miyake, et al., CrySPY: a crystal structure prediction tool accelerated by machine learning, Sci. Technol. Adv. Mater.: Methods 1 (1) (2021) 87–97, https://doi.org/10.1080/27660400.2021.1943171.

[25] J. Wang, H. Gao, Y. Han, C. Ding, S. Pan, Y. Wang, Q. Jia, H.-T. Wang, D. Xing, J. Sun, MAGUS: machine learning and graph theory assisted universal structure searcher, Natl. Sci. Rev. 10 (7) (2023), https://doi.org/10.1093/nsr/nwad128.

[26] S.M. Woodley, R. Catlow, Crystal structure prediction from first principles, Nat. Mater. 7 (12) (2008) 937–946, https://doi.org/10.1038/nmat2321.

[27] A.R. Oganov, A.O. Lyakhov, M. Valle, How evolutionary crystal structure prediction Works—And why, Acc. Chem. Res. 44 (3) (2011) 227–237, https://doi.org/10.1021/ar1001318.

[28] A.R. Oganov, Crystal structure prediction: reflections on present status and challenges, Faraday Discuss 211 (2018) 643–660, https://doi.org/10.1039/C8FD90033G.

[29] D.H. Bowskill, I.J. Sugden, S. Konstantinopoulos, C.S. Adjiman, C.C. Pantelides, Crystal structure prediction methods for organic molecules: state of the art, Annu. Rev. Chem. Biomol. Eng. 12 (1) (2021) 593–623, https://doi.org/10.1146/annurev-chembioeng-060718-030256.

[30] J. Nyman, G.M. Day, Static and lattice vibrational energy differences between polymorphs, CrystEngComm 17 (28) (2015) 5154–5165, https://doi.org/10.1039/C5CE00045A.

[31] G.J.O. Beran, Frontiers of molecular crystal structure prediction for pharmaceuticals and functional organic materials, Chem. Sci. 14 (46) (2023) 13290–13312, https://doi.org/10.1039/D3SC03903J.

[32] F. Taulelle, NMR crystallography: crystallochemical formula and space group selection, Solid State Sci. 6 (10) (2004) 1053–1057, https://doi.org/10.1016/j.solidstatesciences.2004.07.033.

[33] R.K. Harris, NMR crystallography: the use of chemical shifts, Solid State Sci. 6 (10) (2004) 1025–1037, https://doi.org/10.1016/j.solidstatesciences.2004.03.040.

[34] C. Martineau, J. Senker, F. Taulelle, NMR crystallography, Annu. Rep. NMR Spectrosc. 82 (2014) 1–57, https://doi.org/10.1016/B978-0-12-800184-4.00001-1.

[35] C. Martineau, NMR crystallography: applications to inorganic materials, Solid State Nucl. Magn. Reson. 63–64 (2014) 1–12, https://doi.org/10.1016/j.ssnmr.2014.07.001.

[36] P. Hodgkinson, NMR crystallography of molecular organics, Prog. Nucl. Magn. Reson. Spectrosc. 118–119 (2020) 10–53, https://doi.org/10.1016/j.pnmrs.2020.03.001.

[37] F. Taulelle, Fundamental principles of NMR crystallography, in: R.K. Harris, R. E. Wasylishen, M.J. Duer (Eds.), Encyclopedia of Magnetic Resonance, John Wiley & Sons, Ltd, Chichester, UK, 2009, pp. 1–14, https://doi.org/10.1002/9780470034590.emrstm1003.

[38] S.E. Ashbrook, D. McKay, Combining solid-state NMR spectroscopy with first-principles calculations – a guide to NMR crystallography, Chem. Commun. 52 (45) (2016) 7186–7204, https://doi.org/10.1039/C6CC02542K.

[39] D.L. Bryce, NMR crystallography: structure and properties of materials from solid-state nuclear magnetic resonance observables, IUCrJ 4 (4) (2017) 350–359, https://doi.org/10.1107/S2052252517006042.

[40] D.H. Brouwer, J. Van Huizen, NMR crystallography of zeolites: how far can we Go without diffraction data? Magn. Reson. Chem. 57 (5) (2019) 167–175, https://doi.org/10.1002/mrc.4748.

[41] E. Salager, G.M. Day, R.S. Stein, C.J. Pickard, B. Elena, L. Emsley, Powder crystallography by combined crystal structure prediction and high-resolution 1 H solid-state NMR spectroscopy, J. Am. Chem. Soc. 132 (8) (2010) 2564–2566, https://doi.org/10.1021/ja909449k.

[42] M. Baias, J.-N. Dumez, P.H. Svensson, S. Schantz, G.M. Day, L. Emsley, *De Novo* Determination of the Crystal Structure of a Large Drug Molecule by Crystal Structure Prediction-Based Powder NMR Crystallography, J. Am. Chem. Soc. 135 (46) (2013) 17501–17507, https://doi.org/10.1021/ja4088874.

[43] M.K. Dudek, P. Paluch, E. Pindelska, Crystal structures of two furazidin polymorphs revealed by a joint effort of crystal structure prediction and NMR crystallography, Acta Crystallogr. B 76 (3) (2020) 322–335, https://doi.org/10.1107/S205252062000373X.

[44] M. Khalaji, P. Paluch, M.J. Potrzebowski, M.K. Dudek, Narrowing down the conformational space with solid-state NMR in crystal structure prediction of linezolid cocrystals, Solid State Nucl. Magn. Reson. 121 (August) (2022) 101813, https://doi.org/10.1016/j.ssnmr.2022.101813.

[45] K.D.M. Harris, NMR crystallography as a vital tool in assisting crystal structure determination from powder XRD data, Crystals (Basel) 12 (9) (2022) 1277, https://doi.org/10.3390/cryst12091277.

[46] F.M. Paruzzo, A. Hofstetter, F. Musil, S. De, M. Ceriotti, L. Emsley, Chemical shifts in molecular solids by machine learning, Nat. Commun. 9 (1) (2018) 4501, https://doi.org/10.1038/s41467-018-06972-x.

[47] M. Cordova, E.A. Engel, A. Stefaniuk, F. Paruzzo, A. Hofstetter, M. Ceriotti, L. Emsley, A machine learning model of chemical shifts for chemically and structurally diverse molecular solids, J. Phys. Chem. C 126 (39) (2022) 16710–16720, https://doi.org/10.1021/acs.jpcc.2c03854.

[48] A. Hofstetter, M. Balodis, F.M. Paruzzo, C.M. Widdifield, G. Stevanato, A. C. Pinon, P.J. Bygrave, G.M. Day, L. Emsley, Rapid structure determination of molecular solids using chemical shifts directed by unambiguous prior constraints, J. Am. Chem. Soc. 141 (42) (2019) 16624–16634, https://doi.org/10.1021/jacs.9b03908.

[49] M. Balodis, M. Cordova, A. Hofstetter, G.M. Day, L. Emsley, De Novo Crystal Structure Determination from Machine Learned Chemical Shifts, J. Am. Chem. Soc. 144 (16) (2022) 7215–7223, https://doi.org/10.1021/jacs.1c13733.

[50] D. Torodii, J.B. Holmes, P. Moutzouri, S.O. Nilsson Lill, M. Cordova, A.C. Pinon, K. Grohe, S. Wegner, O.D. Putra, S. Norberg, et al., Crystal structure validation of verinurad via proton-detected ultra-fast MAS NMR and machine learning, Faraday Discuss 255 (2025) 143–158, https://doi.org/10.1039/D4FD00076E.

[51] M. Cordova, P. Moutzouri, S.O. Nilsson Lill, A. Cousen, M. Kearns, S.T. Norberg, A. Svensk Ankarberg, J. McCabe, A.C. Pinon, S. Schantz, et al., Atomic-Level structure determination of amorphous molecular solids by NMR, Nat. Commun. 14 (1) (2023) 5138, https://doi.org/10.1038/s41467-023-40853-2.

[52] J.B. Holmes, D. Torodii, M. Balodis, M. Cordova, A. Hofstetter, F. Paruzzo, S. O. Nilsson Lill, E. Eriksson, P. Berruyer, B. Simões de Almeida, et al., Atomic-Level structure of the amorphous drug atuliflapon via NMR crystallography, Faraday Discuss 255 (2025) 342–354, https://doi.org/10.1039/D4FD00078A.

[53] S.E. Ashbrook, S. Sneddon, New methods and applications in solid-state NMR spectroscopy of quadrupolar nuclei, J. Am. Chem. Soc. 136 (44) (2014) 15440–15456, https://doi.org/10.1021/ja504734p.

[54] A.J. Vega, Quadrupolar nuclei in solids, in: D.M. Grant, R.K. Harris (Eds.), Encyclopedia of Magnetic Resonance, John Wiley & Sons, Ltd, Chichester, UK, 2007, pp. 3869–3888, https://doi.org/10.1002/9780470034590.emrstm0431.

[55] J. Autschbach, S. Zheng, R.W. Schurko, Analysis of electric field gradient tensors at quadrupolar nuclei in common structural motifs, Concepts Magn. Reson. 36A (2) (2010) 84–126, https://doi.org/10.1002/cmr.a.20155.

[56] J. Dutour, N. Guillou, C. Huguenard, F. Taulelle, C. Mellot-Draznieks, G. Chiolite Férey, A case Study for combining NMR crystallography, diffraction and structural simulation, Solid State Sci. 6 (10) (2004) 1059–1067, https://doi.org/10.1016/j.solidstatesciences.2004.07.031.

[57] H.J. Jakobsen, A.R. Hove, R.G. Hazell, H. Bildsøe, J. Skibsted, Solid-state 14N MAS NMR of ammonium ions as a spy to structural insights for ammonium salts, Magn. Reson. Chem. 44 (3) (2006) 348–356, https://doi.org/10.1002/mrc.1772.

[58] H. Hamaed, J.M. Pawlowski, B.F.T. Cooper, R. Fu, S.H. Eichhorn, R.W. Schurko, Application of solid-state $^{35}$ Cl NMR to the structural characterization of hydrochloride pharmaceuticals and their polymorphs, J. Am. Chem. Soc. 130 (33) (2008) 11056–11065, https://doi.org/10.1021/ja802486q.

[59] D.L. Bryce, Calcium binding environments probed by 43Ca NMR spectroscopy, Dalton Trans. 39 (37) (2010) 8593, https://doi.org/10.1039/c0dt00416b.

[60] L.A. O'Dell, R.W. Schurko, K.J. Harris, J. Autschbach, C.I. Ratcliffe, Interaction tensors and local dynamics in common structural motifs of nitrogen: a solid-state 14N NMR and DFT study, J. Am. Chem. Soc. 133 (3) (2011) 527–546, https://doi.org/10.1021/ja108181y.

[61] F.A. Perras, D.L. Bryce, Multinuclear magnetic resonance crystallographic structure refinement and cross-validation using experimental and computed electric field gradients: application to Na2Al2B2O7, J. Phys. Chem. C 116 (36) (2012) 19472–19482, https://doi.org/10.1021/jp308273h.

[62] S.L. Veinberg, K.E. Johnston, M.J. Jaroszewicz, B.M. Kispal, C.R. Mireault, T. Kobayashi, M. Pruski, R.W. Schurko, Natural abundance 14N and 15N solid-state NMR of pharmaceuticals and their polymorphs, Phys. Chem. Chem. Phys. 18 (26) (2016) 17713–17730, https://doi.org/10.1039/C6CP02855A.

[63] A.A. Peach, C.H. Fleischer, K. Levin, S.T. Holmes, J.E. Sanchez, R.W. Schurko, Quadrupolar NMR crystallography guided crystal structure prediction (QNMRX-CSP), CrystEngComm 26 (35) (2024) 4782–4803, https://doi.org/10.1039/D3CE01306E.

[64] C.H. Fleischer, S.T. Holmes, K. Levin, S.L. Veinberg, R.W. Schurko, Characterization of ephedrine HCl and pseudoephedrine HCl using quadrupolar NMR crystallography guided crystal structure prediction, Faraday Discuss 255 (2025) 88–118, https://doi.org/10.1039/D4FD00089G.

[65] S.T. Holmes, R.W. Schurko, Refining crystal structures with quadrupolar NMR and dispersion-corrected density functional theory, J. Phys. Chem. C 122 (3) (2018) 1809–1820, https://doi.org/10.1021/acs.jpcc.7b12314.

[66] S.T. Holmes, C.S. Vojvodin, R.W. Schurko, Dispersion-corrected DFT methods for applications in nuclear magnetic resonance crystallography, J. Phys. Chem. A 124 (49) (2020) 10312–10323, https://doi.org/10.1021/acs.jpca.0c06372.

[67] B.A. Klein, D.G. Tkachuk, V.V. Terskikh, V.K. Michaelis, Expanding the NMR toolkit for biological solids: oxygen-17 enriched fmoc-amino acids, New J. Chem. 45 (28) (2021) 12384–12398, https://doi.org/10.1039/d1nj02847b.

[68] D.H. Brouwer, G.D. Enright, Probing local structure in zeolite frameworks: ultrahigh-field NMR measurements and accurate first-principles calculations of zeolite 29Si magnetic shielding tensors, J. Am. Chem. Soc. 130 (10) (2008) 3095–3105, https://doi.org/10.1021/ja077430a.

[69] O.V. Petrov, V. Chlan, J. Rohlíček, J. Demel, J. Veselý, J. Lang, Exploring structural disorders in aluminum-containing metal-organic frameworks: comparison of solid-state 27Al NMR powder spectra to DFT calculations on bulk periodic structures, J. Phys. Chem. C 124 (23) (2020) 12569–12579, https://doi.org/10.1021/acs.jpcc.0c03000.

[70] R.P. Chapman, D.L. Bryce, Application of multinuclear magnetic resonance and gauge-including projector-augmented-wave calculations to the study of solid group 13 chlorides, Phys. Chem. Chem. Phys. 11 (32) (2009) 6987, https://doi.org/10.1039/b906627f.

[71] T. Charpentier, The PAW/GIPAW approach for computing NMR parameters: a new dimension added to NMR study of solids, Solid State Nucl. Magn. Reson. 40 (1) (2011) 1–20, https://doi.org/10.1016/j.ssnmr.2011.04.006.

[72] J.K. Harper, R. Iuliucci, M. Gruber, K. Kalakewich, Refining crystal structures with experimental 13C NMR shift tensors and lattice-including electronic structure methods, CrystEngComm 15 (43) (2013) 8693, https://doi.org/10.1039/c3ce40108a.

[73] B. Alonso, D. Massiot, P. Florian, H.H. Paradies, P. Gaveau, T. Mineva, 14N and 81Br quadrupolar nuclei as sensitive NMR probes of n -Alkyltrimethylammonium bromide crystal structures. An experimental and theoretical study, J. Phys. Chem. B 113 (35) (2009) 11906–11920, https://doi.org/10.1021/jp9027904.

[74] E. Dib, B. Alonso, T.D.F.T.-D. Mineva, Study of 14N nuclear quadrupolar interactions in Tetra- n -Alkyl ammonium halide crystals, J. Phys. Chem. A 118 (19) (2014) 3525–3533, https://doi.org/10.1021/jp502858n.

[75] V. Martins, J. Xu, I. Hung, Z. Gan, C. Gervais, C. Bonhomme, Y. Huang, 17O solid-state NMR at ultrahigh magnetic field of 35.2 T: resolution of inequivalent oxygen sites in different phases of MOF MIL-53(Al), Magn. Reson. Chem. 59 (9–10) (2021) 940–950, https://doi.org/10.1002/mrc.5122.

[76] J. Shen, V. Terskikh, J. Struppe, A. Hassan, M. Monette, I. Hung, Z. Gan, A. Brinkmann, G. Wu, Solid-state 17O NMR study of α-d-Glucose: exploring new frontiers in isotopic labeling, sensitivity enhancement, and NMR crystallography, Chem. Sci. 13 (9) (2022) 2591–2603, https://doi.org/10.1039/D1SC06060K.

[77] E.A. Engel, A. Anelli, A. Hofstetter, F. Paruzzo, L. Emsley, M. Ceriotti, A Bayesian approach to NMR crystal structure determination, Phys. Chem. Chem. Phys. 21 (42) (2019) 23385–23400, https://doi.org/10.1039/C9CP04489B.

[78] L.J. Mueller, Uniform chi-squared model probabilities in NMR crystallography, Faraday Discuss 255 (2025) 203–221, https://doi.org/10.1039/D4FD00114A.

[79] G.M. Sheldrick, SHELXT – integrated space-group and crystal-structure determination, Acta Crystallogr. A 71 (1) (2015) 3–8, https://doi.org/10.1107/S2053273314026370.

[80] G.M. Sheldrick, Crystal structure refinement with SHELXL, Acta Crystallogr. C 71 (1) (2015) 3–8, https://doi.org/10.1107/S2053229614024218.

[81] M.A. Neumann, X-Cell: a novel indexing algorithm for routine tasks and difficult cases, J. Appl. Crystallogr. 36 (2) (2003) 356–365, https://doi.org/10.1107/S0021889802023348.

[82] S.G.J. van Meerten, W.M.J. Franssen, A.P.M. Kentgens, SsNake: a cross-platform open-source NMR data processing and fitting application, J. Magn. Reson. 301 (2019) 56–66, https://doi.org/10.1016/j.jmr.2019.02.006.

[83] E.L. Hahn, Spin echoes, Phys. Rev. 80 (4) (1950) 580–594, https://doi.org/10.1103/PhysRev.80.580.

[84] J.C.C. Chan, Spin echoes in half-integer quadrupole systems, Concepts Magn. Reson. 11 (6) (1999) 363–377, https://doi.org/10.1002/(SICI)1099-0534(1999)11:6<363::AID-CMR2>3.0.CO;2-A.

[85] D.L. Bryce, G.D. Sward, Chlorine-35/37 NMR spectroscopy of solid amino acid hydrochlorides: refinement of hydrogen-bonded proton positions using experiment and theory, J. Phys. Chem. B 110 (51) (2006) 26461–26470, https://doi.org/10.1021/jp065878c.

[86] L.A. O'Dell, R.W. Schurko, QCPMG using adiabatic pulses for faster acquisition of ultra-wideline NMR spectra, Chem. Phys. Lett. 464 (1–3) (2008) 97–102, https://doi.org/10.1016/j.cplett.2008.08.095.

[87] L.A. O'Dell, A.J. Rossini, R.W. Schurko, Acquisition of ultra-wideline NMR spectra from quadrupolar nuclei by frequency stepped WURST–QCPMG, Chem. Phys. Lett. 468 (4–6) (2009) 330–335, https://doi.org/10.1016/j.cplett.2008.12.044.

[88] R. Bhattacharyya, L. Frydman, Quadrupolar nuclear magnetic resonance spectroscopy in solids using frequency-swept echoing pulses, J. Chem. Phys. 127 (19) (2007), https://doi.org/10.1063/1.2793783.

[89] E. Kupce, R. Freeman, Adiabatic pulses for wideband inversion and broadband decoupling, J. Magn. Reson. 115 (2) (1995) 273–276, https://doi.org/10.1006/jmra.1995.1179.

[90] D. Massiot, I. Farnan, N. Gautier, D. Trumeau, A. Trokiner, J.P. Coutures, 71Ga and 69Ga nuclear magnetic resonance study of β-Ga2O3: resolution of Four- and six-fold coordinated Ga sites in static conditions, Solid State Nucl. Magn. Reson. 4 (4) (1995) 241–248, https://doi.org/10.1016/0926-2040(95)00002-8.

[91] S.L. Veinberg, A.W. Lindquist, M.J. Jaroszewicz, R.W. Schurko, Practical considerations for the acquisition of ultra-wideline 14N NMR spectra, Solid State Nucl. Magn. Reson. 84 (November) (2017) 45–58, https://doi.org/10.1016/j.ssnmr.2016.12.008.

[92] O.B. Peersen, X.L. Wu, I. Kustanovich, S.O. Smith, Variable-amplitude cross-polarization MAS NMR, J. Magn. Reson. 104 (3) (1993) 334–339, https://doi.org/10.1006/jmra.1993.1231.

[93] G. Metz, X.L. Wu, S.O. Smith, Ramped-amplitude cross polarization in magic-angle-spinning NMR, J. Magn. Reson. 110 (2) (1994) 219–227, https://doi.org/10.1006/jmra.1994.1208.

[94] J. Schaefer, E.O. Stejskal, Carbon-13 nuclear magnetic resonance of polymers spinning at the magic angle, J. Am. Chem. Soc. 98 (4) (1976) 1031–1032, https://doi.org/10.1021/ja00420a036.

[95] A. Pines, M.G. Gibby, J.S. Waugh, Proton-enhanced nuclear induction spectroscopy 13C chemical shielding anisotropy in some organic solids, Chem. Phys. Lett. 15 (3) (1972) 373–376, https://doi.org/10.1016/0009-2614(72)80191-X.

[96] A. Pines, M.G. Gibby, J.S. Waugh, Proton-enhanced NMR of dilute spins in solids, J. Chem. Phys. 59 (2) (1973) 569–590, https://doi.org/10.1063/1.1680061.

[97] R.E. Taylor, 13C CP/MAS: application to glycine, Concepts Magn. Reson. 22A (2) (2004) 79–89, https://doi.org/10.1002/cmr.a.20015.

[98] R.L.C. Akkermans, N.A. Spenley, S.H. Robertson, Monte carlo methods in materials studio, Mol. Simul. 39 (14–15) (2013) 1153–1164, https://doi.org/10.1080/08927022.2013.843775.

[99] S.J. Clark, M.D. Segall, C.J. Pickard, P.J. Hasnip, M.I.J. Probert, K. Refson, M. C. Payne, First principles methods using CASTEP, Z. Kristallogr. 220 (5–6) (2005) 567–570, https://doi.org/10.1524/zkri.220.5.567.65075.

[100] S.L. Mayo, B.D. Olafson, W.A. Goddard, DREIDING: a generic force field for molecular simulations, J. Phys. Chem. 94 (26) (1990) 8897–8909, https://doi.org/10.1021/j100389a010.

[101] E. van Lenthe, J.G. Snijders, E.J. Baerends, The zero-order regular approximation for relativistic effects: the effect of spin–orbit coupling in closed shell molecules, J. Chem. Phys. 105 (15) (1996) 6505–6516, https://doi.org/10.1063/1.472460.

[102] J.R. Yates, C.J. Pickard, F. Mauri, Calculation of NMR chemical shifts for extended systems using ultrasoft pseudopotentials, Phys. Rev. B 76 (2) (2007) 024401, https://doi.org/10.1103/PhysRevB.76.024401.

[103] H.J. Monkhorst, J.D. Pack, Special points for brillouin-zone integrations, Phys. Rev. B 13 (12) (1976) 5188–5192, https://doi.org/10.1103/PhysRevB.13.5188.

[104] B.G. Pfrommer, M. Côté, S.G. Louie, M.L. Cohen, Relaxation of crystals with the quasi-newton method, J. Comput. Phys. 131 (1) (1997) 233–240, https://doi.org/10.1006/jcph.1996.5612.

[105] C.J. Pickard, F. Mauri, All-electron magnetic response with pseudopotentials: NMR chemical shifts, Phys. Rev. B 63 (24) (2001) 245101, https://doi.org/10.1103/PhysRevB.63.245101.

[106] K. Oda, H. Koyama, A refinement of the crystal structure of histidine hydrochloride monohydrate, Acta Crystallogr. B 28 (2) (1972) 639–642, https://doi.org/10.1107/S0567740872002894.
[107] M.A. Pinard, K. Aslan, Metal-assisted and microwave-accelerated evaporative crystallization, Cryst. Growth Des. 10 (11) (2010) 4706–4709, https://doi.org/10.1021/cg101059c.
[108] A. Dawson, D.R. Allan, S.A. Belmonte, S.J. Clark, W.I.F. David, P.A. McGregor, S. Parsons, C.R. Pulham, L. Sawyer, Effect of high pressure on the crystal structures of polymorphs of glycine, Cryst. Growth Des. 5 (4) (2005) 1415–1427, https://doi.org/10.1021/cg049716m.
[109] S. Chandrasekhar, R. Hota, A.R. Choudhury, T. N. G. R. CCDC 223378: experimental crystal structure determination, CSD Comm. (2003), https://doi.org/10.5517/cc7hfrw.
[110] M. Strohmeier, D. Stueber, D.M. Grant, Accurate 13C and 15N chemical shift and 14N quadrupolar coupling constant calculations in amino acid crystals: Zwitterionic, hydrogen-bonded systems, J. Phys. Chem. A 107 (38) (2003) 7629–7642, https://doi.org/10.1021/jp0350114.
[111] P. Pyykkö, Year-2017 nuclear Quadrupole moments, Mol. Phys. 116 (10) (2018) 1328–1338, https://doi.org/10.1080/00268976.2018.1426131.
[112] B. Ganguly, M.K. Kesharwani, N. Basarić, E. Suresh, A.K. Biswas, K. Mlinarić-Majerski, Conformational preference of glycinamide in solution: an answer derived from combined experimental and computational studies, J. Mol. Graph. Model. 46 (2013) 52–58, https://doi.org/10.1016/j.jmgm.2013.09.007.
[113] D. Vušak, N. Smrečki, B. Prugovečki, I. Đilović, I. Kirasić, D. Žilić, S. Muratović, D. Matković-Čalogović, Cobalt, nickel and copper complexes with glycinamide: structural insights and magnetic properties, RSC Adv. 9 (38) (2019) 21637–21645, https://doi.org/10.1039/C9RA03693H.
[114] A.R. Al-Karaghouli, F.E. Cole, M.S. Lehmann, C.R. Miskell, J.J. Verbist, T. F. Koetzle, Precision neutron diffraction structure determination of protein and nucleic acid components. XVII. Molecular and crystal structure of the amino acid glycine hydrochloride, J. Chem. Phys. 63 (4) (1975) 1360–1366, https://doi.org/10.1063/1.431523.
[115] B. Di Blasio, V. Pavone, C. Pedone, Ccdc 1169411: experimental crystal structure determination, CSD Comm. 6 (4) (1977) 745–748.
[116] F.H. Allen, The Cambridge structural database: a quarter of a million crystal structures and rising, Acta Crystallogr. B 58 (3) (2002) 380–388, https://doi.org/10.1107/S0108768102003890.
[117] G. Barr, W. Dong, C.J. Gilmore, A. Kern, A. Parkin, C.C. Wilson, Using the Cambridge structural database to validate powder structures, Z. Kristallogr. 2007 (suppl_26) (2007) 209–214, https://doi.org/10.1524/zkri.2007.2007.suppl_26.209.
[118] L. Wang, J.K. Harper, Refining crystal structures using 13C NMR chemical shift tensors as a target function, CrystEngComm 23 (40) (2021) 7061–7071, https://doi.org/10.1039/D1CE00960E.
[119] H.G. Brittain, Polymorphism in Pharmaceutical Solids; Informa Healthcare USA, Inc: New York, NY, 2009.
[120] N.K. Thakral, R.L. Zanon, R.C. Kelly, S. Thakral, Applications of powder X-Ray diffraction in small molecule pharmaceuticals: achievements and aspirations, J. Pharmacol. Sci. 107 (12) (2018) 2969–2982, https://doi.org/10.1016/j.xphs.2018.08.010.
[121] M. Zilka, D.V. Dudenko, C.E. Hughes, P.A. Williams, S. Sturniolo, W.T. Franks, C. J. Pickard, J.R. Yates, K.D.M. Harris, S.P. Brown, Ab initio random structure searching of organic molecular solids: assessment and validation against experimental data, Phys. Chem. Chem. Phys. 19 (38) (2017) 25949–25960, https://doi.org/10.1039/c7cp04186a.
[122] G. Desiraju, T. Steiner, The Weak Hydrogen Bond, vol. 9, Oxford University Press, Oxford, England, 2001, https://doi.org/10.1093/acprof:oso/9780198509707.001.0001.
[123] M. Hildebrand, H. Hamaed, A.M. Namespetra, J.M. Donohue, R. Fu, I. Hung, Z. Gan, R.W. Schurko, 35Cl solid-state NMR of HCl salts of active pharmaceutical ingredients: structural prediction, spectral fingerprinting and polymorph recognition, CrystEngComm 16 (31) (2014) 7334–7356, https://doi.org/10.1039/c4ce00544a.
[124] S.T. Holmes, J.M. Hook, R.W. Schurko, Nutraceuticals in bulk and dosage forms: analysis by 35Cl and 14N solid-state NMR and DFT calculations, Mol. Pharm. 19 (2) (2022) 440–455, https://doi.org/10.1021/acs.molpharmaceut.1c00708.
[125] C.S. Vojvodin, S.T. Holmes, L.K. Watanabe, J.M. Rawson, R.W. Schurko, Multi-component crystals containing urea: mechanochemical synthesis and characterization by 35Cl solid-state NMR spectroscopy and DFT calculations, CrystEngComm 24 (14) (2022) 2626–2641, https://doi.org/10.1039/D1CE01610E.
[126] Z.T. Dowdell, A.A. Peach, J.P. Purdie, S.T. Holmes, L.K. Watanabe, J.M. Rawson, R.W. Schurko, Mechanochemical synthesis and 35Cl NMR crystallography of ionic cocrystals of phenothiazine drugs, CrystEngComm (2025), https://doi.org/10.1039/d5ce00426h.
[127] Z. Rehman, W.T. Franks, B. Nguyen, H.F. Schmidt, G. Scrivens, S.P. Brown, Discovering the solid-state secrets of lorlatinib by NMR crystallography: to hydrogen bond or not to hydrogen bond, J. Pharmacol. Sci. 112 (7) (2023) 1915–1928, https://doi.org/10.1016/j.xphs.2023.02.022.
[128] Z. Rehman, J. Lubay, W.T. Franks, A.P. Bartók, E.K. Corlett, B. Nguyen, G. Scrivens, B.M. Samas, H. Frericks-Schmidt, S.P. Brown, Organic NMR crystallography: enabling progress for applications to pharmaceuticals and plant cell walls, Faraday Discuss 255 (2024) 222–243, https://doi.org/10.1039/d4fd00088a.
[129] S.T. Holmes, J.M. Hook, R.W. Schurko, Nutraceuticals in bulk and dosage forms: analysis by 35Cl and 14N solid-state NMR and DFT calculations, Mol. Pharm. 19 (2) (2022) 440–455, https://doi.org/10.1021/acs.molpharmaceut.1c00708.
[130] R.K. Harris, A.C. Olivieri, Quadrupolar effects transferred to Spin- 1 2 magic-angle spinning spectra of solids, Prog. Nucl. Magn. Reson. Spectrosc. 24 (5) (1992) 435–456, https://doi.org/10.1016/0079-6565(92)80004-Y.
[131] B.H.R. Toby, Factors in rietveld analysis: how good is good enough? Powder Diffr. 21 (1) (2006) 67–70, https://doi.org/10.1154/1.2179804.
[132] W. Clegg, X-Ray Crystallography, Oxford University Press, Oxford, U.K., 2015.
[133] D.M. Grant, F. Liu, R.J. Iuliucci, C.G. Phung, J.C. Facelli, D.W. Alderman, Relationship of 13C NMR chemical shift tensors to diffraction structures, Acta Crystallogr. B 51 (4) (1995) 540–546, https://doi.org/10.1107/S0108768195000383.
[134] R. Toomey, L. Wang, E.C. Heider, J.D. Hartman, A.J. Nichols, D.A.A. Myles, A. S. Gardberg, G.J. McIntyre, M. Zeller, M.A. Mehta, et al., NMR-guided refinement of crystal structures using 15N chemical shift tensors, CrystEngComm 26 (25) (2024) 3289–3302, https://doi.org/10.1039/d4ce00237g.
[135] S.T. Holmes, R.J. Iuliucci, K.T. Mueller, C. Dybowski, Semi-empirical refinements of crystal structures using 17O quadrupolar-coupling tensors, J. Chem. Phys. 146 (6) (2017) 64201, https://doi.org/10.1063/1.4975170.
[136] S. Grimme, J. Antony, S. Ehrlich, H. Krieg, A consistent and accurate Ab initio parametrization of density functional dispersion correction (DFT-D) for the 94 elements H-Pu, J. Chem. Phys. 132 (15) (2010), https://doi.org/10.1063/1.3382344.
[137] S. Grimme, S. Ehrlich, L. Goerigk, Effect of the damping function in dispersion corrected density functional theory, J. Comput. Chem. 32 (7) (2011) 1456–1465, https://doi.org/10.1002/jcc.21759.
[138] E. Caldeweyher, C. Bannwarth, S. Grimme, Extension of the D3 dispersion coefficient model, J. Chem. Phys. 147 (3) (2017), https://doi.org/10.1063/1.4993215, 0–7.